



# Highly efficient degradation of basic dyes using gold-coated nature-based supermagnetic iron oxide nanoparticles as eco-friendly nanocatalysts

Ghassan H. Matar<sup>1</sup> · Muberra Andac<sup>1,2</sup>

Received: 13 December 2023 / Accepted: 1 March 2024 / Published online: 9 March 2024  
© The Author(s) 2024

## Abstract

Nowadays, organic dyes are prevalent components in wastewater discharges due to their extensive use in various industries, posing a significant threat to public health across different organisms. As a result, wastewater treatment has become an indispensable requirement. In this study, we synthesized supermagnetic iron oxide (Fe<sub>3</sub>O<sub>4</sub> NPs) and gold-iron oxide bimetallic nanoparticles (Au@Fe<sub>3</sub>O<sub>4</sub> BNPs) using an eco-friendly method that involved natural compounds extracted from brown Egyptian propolis. We employed UV-visible spectroscopy, FTIR, XRD, VSM, SEM, HRTEM, EDX, Zeta potential and XPS techniques to examine the optical characteristics, chemical structure, crystalline structure, magnetic properties, morphology, size, and chemical composition of these biosynthesized nanoparticles. Furthermore, these nanoparticles were used as nanocatalysts for the removal of cationic dyes. The photocatalytic results indicated high efficiency in the removal of methylene blue (MB), crystal violet (CV), and malachite green (MG) dyes from aqueous solutions using Fe<sub>3</sub>O<sub>4</sub> NPs and Au@Fe<sub>3</sub>O<sub>4</sub> BNPs. The removal rates of MB, CV, and MG were about 95.2% in 70 min, 99.4% in 50 min, and 96.2% in 60 min for Fe<sub>3</sub>O<sub>4</sub> NPs, and 97.1% in 50 min, 99.1% in 30 min, and 98.1% in 50 min for Au@Fe<sub>3</sub>O<sub>4</sub> BNPs, respectively. The study also assessed the potential anti-radical properties of the extract, Fe<sub>3</sub>O<sub>4</sub> NPs, and Au@Fe<sub>3</sub>O<sub>4</sub> BNPs using the DPPH assay, and the results demonstrated their antioxidant activity. Finally, these Fe<sub>3</sub>O<sub>4</sub> NPs and Au@Fe<sub>3</sub>O<sub>4</sub> BNPs have the potential to serve as efficient antioxidants and photocatalysts for removing basic dyes from water.

**Keywords** Green synthesis · Supermagnetic · Iron oxide nanoparticles · Gold-iron oxide bimetallic · Photocatalytic activity · Radical scavenging

## Introduction

Water resources, particularly groundwater, have become contaminated due to natural and artificial factors, as well as the release of various pollutants from different sources. Among the pollutants, dyes have emerged as a major concern, commonly carried by effluents from various industries,

especially the textile industry (Kumar et al. 2022). Methylene blue (MB), crystal violet (CV), and malachite green (MG) are synthetic dyes widely employed in various industrial and laboratory applications (Oladoye et al. 2022). Despite their versatility and utility, these dyes have raised significant environmental concerns due to their potential to cause harm to ecosystems. MB and CV, when released into the environment through textile and industrial processes, can have adverse effects on water quality and aquatic life (Mani and Bharagava 2016). In particular, MG has been associated with environmental damage when used in aquaculture to treat fish diseases, as it can persist in aquatic environments and accumulate in fish tissues, posing risks to both aquatic organisms and human consumers (Kwan et al. 2020).

To minimize the risks of these diseases, it is essential to eliminate these pollutants from the water. Studies have revealed that untreated industrial effluents are one of the primary sources of these contaminants, which significantly

Responsible Editor: George Z. Kyzas

✉ Ghassan H. Matar  
ghassanhaz8@gmail.com

Muberra Andac  
mandac@omu.edu.tr

<sup>1</sup> Department of Chemistry, Ondokuz Mayıs University, Samsun, Turkey

<sup>2</sup> Department of Nanoscience and Nanotechnology, Ondokuz Mayıs University, Samsun, Turkey

affect the ecosystem and living organisms. Several technologies, time-consuming and non-destructive, are currently employed such as ion-exchange, adsorption, chemical precipitation, and membrane systems (Ahmed et al. 2022; Younas et al. 2021). Therefore, scientists are now developing environment-efficient technologies by using nanomaterials that demonstrate extensive potential for degrading hazardous organic dyes in water-based environments.

Nanotechnology as a highly concerned technology is increasingly used in environmental care (Shinde et al. 2023). In recent times, magnetic nanoparticles (MNPs) and bimetallic nanoparticles (BNPs) have gained significant attention due to their supermagnetic characteristics resulting from their small size (Idris and Roy 2023). These magnetic properties allow the potential use of these materials in eliminating and controlling environmental pollutants, as well as in the purification and prevention of their dispersion. Magnetite ( $\text{Fe}_3\text{O}_4$ ) serves as an illustrative instance within this category and finds widespread use due to its robust magnetic attributes, expansive surface area, and limited toxicity, rendering it suitable for applications in both biomedicine and environmental remediation (Díez et al. 2022). These characteristics are contingent upon the methodology employed in the synthesis of MNPs, as it governs their dimensions, size distribution, shape, and consequently, their magnetic behavior. The characteristics of BNPs are influenced by various factors, including the type of reducing agents employed, the redox potentials of the metal ions, and van der Waals attractions among metal atoms (S. Ali et al. 2021). These factors determine whether BNPs will take on configurations such as core-shell, hetero-structure, multi-shell, cluster-in-cluster, or random alloy (Sharma et al. 2019). Additionally, the synthesis method used can impact the crystal structure and distribution of metal ions within the BNPs (F. Ali et al. 2023; N. Zhang et al. 2021). Consequently, the development and utilization of MNPs and BNPs, represent a promising avenue in the quest to address environmental challenges and advance various applications in environmental care (Cheng et al. 2023) and biomedicine (Allam et al. 2021).

Lately, there has been significant interest in the scientific community regarding green synthetic routes for producing nanoparticles (NPs). Many case studies focusing on green synthesis emphasize the use of methods and reagents that minimize the need for toxic reagents, solvents, or by-products during NPs preparation (Devi et al. 2023). The green approach, utilizing bio-active compounds and phytochemicals found in natural biomass, especially plant-based biomass like leaves, flowers, and flowers, has become the most commonly adopted method for preparing and stabilizing NPs (Laib et al. 2023; Rahman et al. 2022). This approach is straightforward, cost-effective, environmentally friendly, and safe for human use, making it highly advantageous for

diverse NPs applications. Furthermore, being a one-step process, it also facilitates large-scale production.

Brown Egyptian propolis, derived from resinous substances collected by honeybees from various plant sources in Egypt, has garnered increasing attention for its diverse applications and numerous advantages. This type of propolis contains a complex mixture of bioactive compounds, including flavonoids, phenolic acids, and terpenes, which contribute to its potent antioxidant, antimicrobial, and anti-inflammatory properties (Matar and Andac 2023; Mohamed et al. 2022). These bioactive constituents have been harnessed for medicinal and therapeutic purposes, particularly in traditional and complementary medicine. However, the bio-fabrication of supermagnetic iron oxide nanoparticles ( $\text{Fe}_3\text{O}_4$  NPs) and gold-iron oxide bimetallic nanoparticles ( $\text{Au}@Fe_3O_4$  BNPs) using propolis extract has not been previously documented.

The current study was designed to address this gap by synthesizing  $\text{Fe}_3\text{O}_4$  NPs and  $\text{Au}@Fe_3O_4$  BNPs using Egyptian propolis extract. The synthesized  $\text{Fe}_3\text{O}_4$  NPs and  $\text{Au}@Fe_3O_4$  BNPs were then thoroughly characterized to confirm their particle size, morphology, crystallite size, particle composition, functional groups on the particle surface, and magnetic properties. Also, their photocatalytic potential for degrading basic dyes such as MB, CV, and MG dye as well as antiradical potential were tested. The successful utilization of propolis extract in synthesizing NPs could pave the way for further advancements and discoveries, making these NPs highly versatile for diverse applications in different scientific domains.

## Materials and methods

### Materials

The propolis samples were collected in the delta region, Egypt. Iron (III) chloride hexahydrate ( $\text{FeCl}_3 \cdot 6\text{H}_2\text{O}$ ), Iron (II) chloride tetrahydrate ( $\text{FeCl}_2 \cdot 4\text{H}_2\text{O}$ ), ammonium hydroxide solution ( $\text{NH}_4\text{OH}$ , 28%), Tetrachloroauric (III) acid ( $\text{HAuCl}_4 \cdot 3\text{H}_2\text{O}$ ), and DPPH (1,1-Diphenyl-2-picryl-hydrazyl) were purchased from Sigma-Aldrich, USA. MB, CV, and MG were purchased from INTERLAB Laboratory Products, Turkey. Deionized water was used in all experiments.

### Green synthesis of AuNPs, $\text{Fe}_3\text{O}_4$ NPs, and $\text{Au}@Fe_3O_4$ BNPs

Green synthesis of monometallic and BNPs using propolis extract involves the use of natural compounds present in propolis as reducing and stabilizing agents.

### Fe<sub>3</sub>O<sub>4</sub> NPs biosynthesis

Initially, a propolis extract was prepared using a 90% ethanol solvent at a 1:10 (w/v) ratio, according to our previous work (Matar and Andac 2023). Regarding the biosynthesis of supermagnetic Fe<sub>3</sub>O<sub>4</sub> NPs, 5 mL of the extract was added to 50 mL of FeCl<sub>3</sub>·6H<sub>2</sub>O (0.2M) and FeCl<sub>2</sub>·4H<sub>2</sub>O (0.1M) solutions. The yellowish-colored solution turned black with the addition of extract. Subsequently, 5 mL of NH<sub>4</sub>OH (28%) was added dropwise, and the solution was vigorously stirred for 1 h. The precipitated Fe<sub>3</sub>O<sub>4</sub> NPs were collected using a magnet, washed with deionized water several times, and then dried at 50 °C in an oven. Later, the powder Fe<sub>3</sub>O<sub>4</sub> NPs was stored at room temperature for further use. The following experimental steps for the biosynthesis of Fe<sub>3</sub>O<sub>4</sub> NPs using propolis extract are presented in Fig. S1 (see Supplementary Material).

### AuNPs biosynthesis

For propolis extract-mediated biosynthesis of AuNPs, 1 mL of the extract was added to a solution of HAuCl<sub>4</sub>·xH<sub>2</sub>O (1 mM, 50 mL), and the mixture was stirred and heated at 45 °C. The reducing agents present in the extract convert the gold ions into AuNPs as evidenced by the change in color of the solution to color dark purple. The synthesized AuNPs were washed three times with deionized water and then centrifuged at 8000 rpm for 15 min to remove unreacted biomolecules. Finally, the optimum time for green synthesis of

AuNPs was recorded at 90 min. After that, the AuNPs were dried and stored at room temperature for further use.

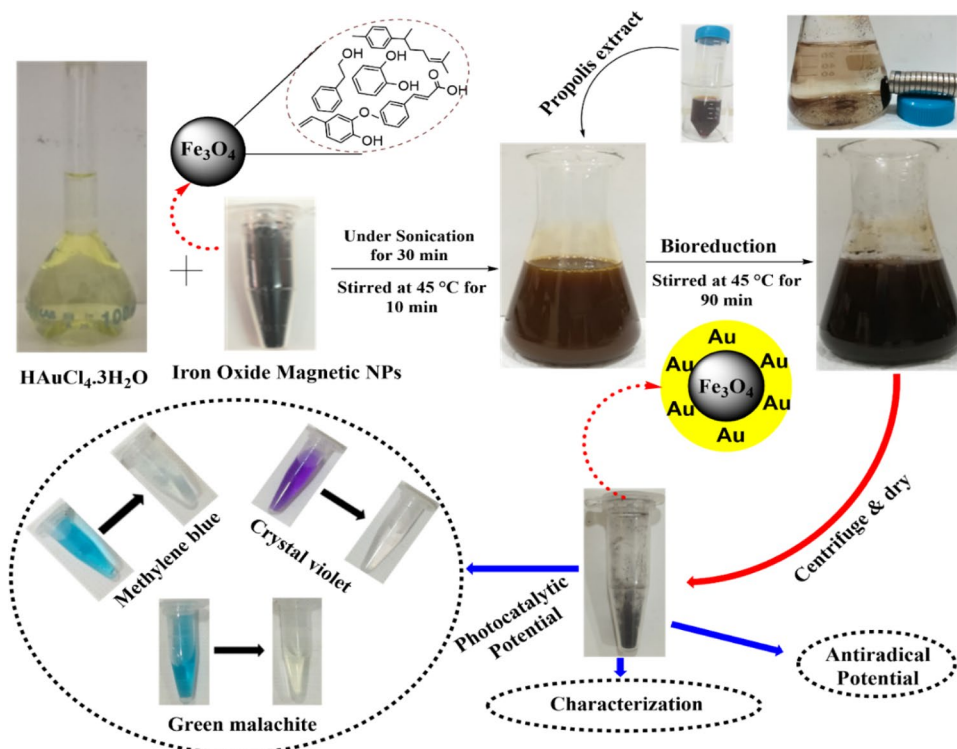
### Synthesis of Au@Fe<sub>3</sub>O<sub>4</sub> BNPs

Fe<sub>3</sub>O<sub>4</sub> NPs synthesized as described in the previous step was used in the synthesis of Au@Fe<sub>3</sub>O<sub>4</sub> BNPs. To achieve this, 0.1 g of the prepared Fe<sub>3</sub>O<sub>4</sub> NPs was mixed with a 100 mL aqueous solution of 1 mM HAuCl<sub>4</sub>·3H<sub>2</sub>O under sonication for 30 min. The resulting brown-colored dispersion of Fe<sub>3</sub>O<sub>4</sub> NPs in HAuCl<sub>4</sub>·3H<sub>2</sub>O solution was vigorously stirred at 45 °C for 10 min. 2 mL of propolis extract was then added drop by drop to the mixture, reducing the gold ions into AuNPs. The reaction was allowed to stir at 45 °C for 90 min. The brownish color solution changed to reddish-brown, indicating the formation and coating of AuNPs on the surface of the Fe<sub>3</sub>O<sub>4</sub> NPs. After the synthesized Au@Fe<sub>3</sub>O<sub>4</sub> BNPs were collected by a magnet, they were washed three times with deionized water and subsequently dried for further use. The following experimental steps for the biosynthesis of Au@Fe<sub>3</sub>O<sub>4</sub> BNPs using propolis extract are shown in Fig. 1.

### Characterizations

The synthesis of Fe<sub>3</sub>O<sub>4</sub> NPs, AuNPs, and Au@Fe<sub>3</sub>O<sub>4</sub> BNPs, as well as their photocatalytic activities, were monitored by UV-visible spectroscopy (Thermo Scientific™, USA) at a wavelength ranging from 200–800 nm. FTIR spectroscopy (Perkin-Elmer Spectrum Two FT-IR) was used to determine

**Fig. 1** Schematic representation of the green synthesis of Au@Fe<sub>3</sub>O<sub>4</sub> BNPs using propolis extract



functional groups on the surface of the Fe<sub>3</sub>O<sub>4</sub> NPs, AuNPs and Au@Fe<sub>3</sub>O<sub>4</sub> BNPs at wavelengths of 4000 – 400 cm<sup>-1</sup>. FE-SEM images (JEOL-JSM-7001F, Japan) and HR-TEM images (FEI TALOS F200S TEM 200 kV, USA) were deployed to examine the morphology and size of NPs. The elemental composition of surveyed samples was measured with EDX spectra (Oxford X-Max 80 mm<sup>2</sup>, UK). The crystalline structure of the Fe<sub>3</sub>O<sub>4</sub> NPs and Au@Fe<sub>3</sub>O<sub>4</sub> BNPs powder sample was measured using XRD (Rigaku Smart Lab X-ray diffractometer with monochromatic Cu K $\alpha$  radiation, Japan) at 2 $\theta$  ranging from 10° to 80°. The zeta potential of the Fe<sub>3</sub>O<sub>4</sub> NPs and Au@Fe<sub>3</sub>O<sub>4</sub> NPs was carried out by the zeta sizer instrument (Malvern Zetasizer equipped with MPT-2 Titrator, Nano ZS). The Fe<sub>3</sub>O<sub>4</sub> NPs and Au@Fe<sub>3</sub>O<sub>4</sub> BNPs powder sample were analyzed using a vibrating sample magnetometer (VSM) with the model Dexing Magnet VSM 550. The magnetization curve was recorded at room temperature. The chemical state of Fe<sub>3</sub>O<sub>4</sub> NPs and Au@Fe<sub>3</sub>O<sub>4</sub> BNPs was investigated using X-ray photoelectron spectroscopy (XPS, Thermo Scientific K-Alpha, USA).

### Photocatalytic degradation performance of basic dyes

The photocatalytic activities of MB, CV, and MG dyes on Fe<sub>3</sub>O<sub>4</sub> NPs and Au@Fe<sub>3</sub>O<sub>4</sub> BNPs were studied under direct light exposure. Typically, 10 mg of Fe<sub>3</sub>O<sub>4</sub> NPs and Au@Fe<sub>3</sub>O<sub>4</sub> BNPs were added to each of the dye solutions (10 mL, 10 ppm) without the addition of any catalyst. Subsequently, the reaction system was irradiated under visible light (a FCL 22W Daylight fluorescent lamp). The mixture was sampled every 10 min and collected using magnets. A UV-Vis spectrophotometer was used to examine the absorbance of the supernatant obtained with the magnets. Meanwhile, we performed the sorption process of dyes by keeping the mixtures in the dark for the same duration as the removal efficiency time observed in photodegradation for each dye. The degradation efficiency (%) was determined based on the maximum degradation of MB, CV, and MG dye solutions at 665 nm, 580 nm, and 618 nm, respectively. The efficiency of dye degradation was evaluated by applying equation (1).

$$\text{Degradation efficiency (\%)} = \left( \frac{A_0 - A}{A_0} \right) \times 100 \quad (1)$$

Here, A<sub>0</sub> and A are the absorbance of dye before and after photo-irradiation, respectively.

### Antioxidant activity

The antioxidant activities of propolis extract, Fe<sub>3</sub>O<sub>4</sub> NPs, and Au@Fe<sub>3</sub>O<sub>4</sub> BNPs were evaluated using the DPPH free radical scavenging assay. In this assay, 0.5 mL of the propolis extract, Fe<sub>3</sub>O<sub>4</sub> NPs, and Au@Fe<sub>3</sub>O<sub>4</sub> BNPs at

concentrations ranging from 20 to 100  $\mu\text{g/mL}$  were mixed with 1 mL of a 0.1 mM DPPH solution. These mixtures were then incubated in darkness for 30 min. After incubation, the absorbance of these mixtures was measured at a wavelength of 517 nm. As a standard, ascorbic acid was used at the same concentration range. The percentage of free radical inhibition was determined using the following formula (2):

$$\text{DPPH scavenging ability (\%)} = \left( \frac{A_c - A_s}{A_c} \right) \times 100 \quad (2)$$

Here, A<sub>c</sub> and A<sub>s</sub> are the absorbance of control and after incubation of sample, respectively.

## Results and Discussion

### UV-visible spectrum analysis

Figure 2 displays the UV-visible absorption spectrum of the propolis extract, Fe<sub>3</sub>O<sub>4</sub> NPs, AuNPs, and Au@Fe<sub>3</sub>O<sub>4</sub> BNPs. The UV-visible spectrum of the propolis extract exhibited a characteristic absorption peak at 270 nm (Fig. 2a), indicating the presence of phenolic and flavonoid compounds in the extract (Matar and Andac 2023). In contrast, the spectrum of Fe<sub>3</sub>O<sub>4</sub> NPs (Fig. 2b) displayed no discernible absorption peak within the measured wavelength range, consistent with previous reports (Desai et al. 2023). To investigate the influence of incubation time on AuNPs synthesis, we monitored the UV-visible spectra at various time intervals (Fig. 2c). Remarkably, we observed a clear trend of increasing surface plasmon resonance (SPR) peak intensity with prolonged incubation time. The highest intensity of the SPR peak, recorded at a wavelength of 547 nm, was achieved at 90 min of incubation, which is consistent with previous reports (Abdelsattar et al. 2022). This result indicates that the synthesis of AuNPs was completed within 90 min, along with the associated processes of reduction and stabilization. In the spectrum of Au@Fe<sub>3</sub>O<sub>4</sub> BNPs, the SPR peak was notably shifted to a longer wavelength (564 nm), confirming the successful synthesis of these BNPs, with the absorption peak consistent with the presence of AuNPs (Fig. 2d). This shift in the absorption of Au@Fe<sub>3</sub>O<sub>4</sub> BNPs can be attributed to the attachment of AuNPs to Fe<sub>3</sub>O<sub>4</sub> NPs. Furthermore, when we applied a magnetic field, both Fe<sub>3</sub>O<sub>4</sub> NPs and Au@Fe<sub>3</sub>O<sub>4</sub> BNPs displayed attraction towards the magnet (as shown in Fig. 1). This magnetic behavior, along with the shift in the characteristic peak from 547 to 564 nm, collectively confirmed the synthesis of Au@Fe<sub>3</sub>O<sub>4</sub> BNPs. These findings align with prior research in the field, where a redshift in the SPR peak of Au@Fe<sub>3</sub>O<sub>4</sub> BNPs is attributed to the dielectric properties of the Fe<sub>3</sub>O<sub>4</sub> NPs (Desai et al. 2023).



**Fig. 2.** UV-visible spectrum of (a) the propolis extract, (b)  $\text{Fe}_3\text{O}_4$  NPs, (c) the effect of reaction time on the green synthesis of AuNPs, and (d)  $\text{Au}@ \text{Fe}_3\text{O}_4$  BNPs

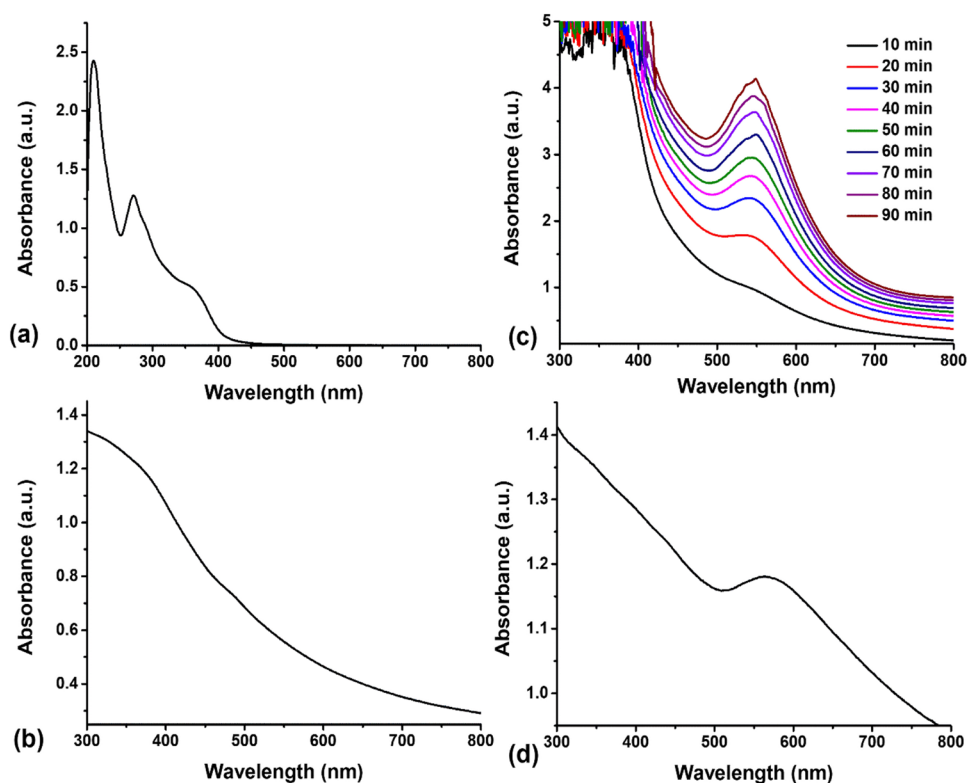
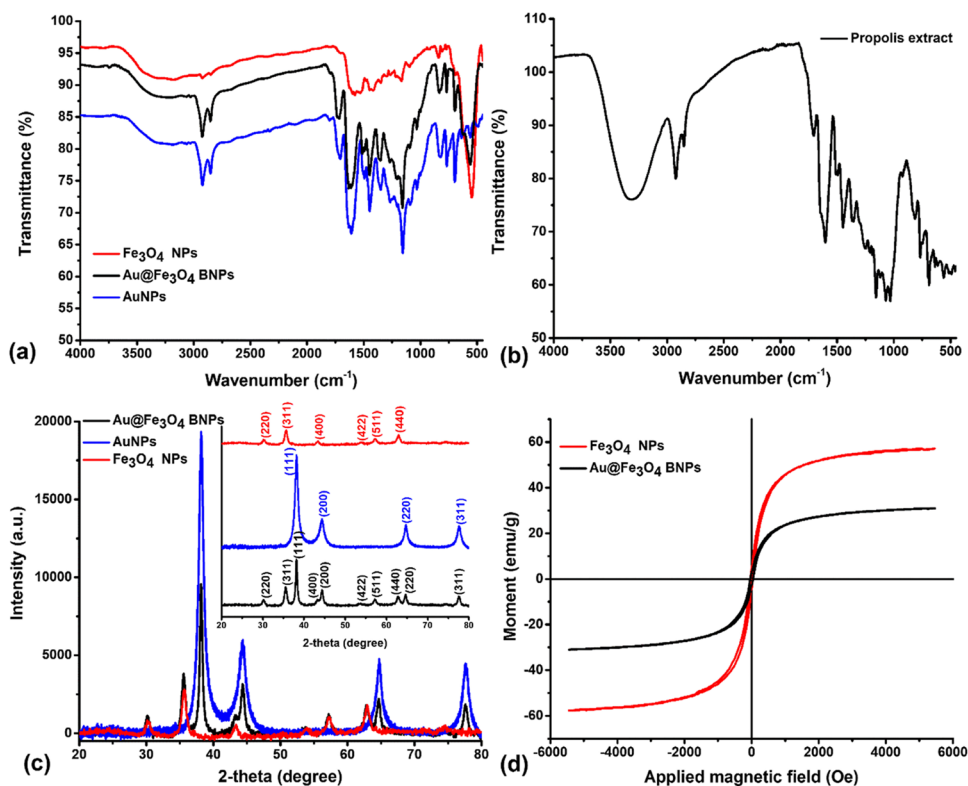


**Fig. 3** (a) FTIR spectra of purified  $\text{Fe}_3\text{O}_4$  NPs, AuNPs and  $\text{Au}@ \text{Fe}_3\text{O}_4$  BNPs, (b) FTIR spectra of propolis extract, (c) XRD patterns of  $\text{Fe}_3\text{O}_4$  NPs, AuNPs and  $\text{Au}@ \text{Fe}_3\text{O}_4$  BNPs, and (d) VSM analysis of  $\text{Fe}_3\text{O}_4$  NPs and  $\text{Au}@ \text{Fe}_3\text{O}_4$  BNPs



## FTIR spectroscopy

The FTIR spectra of propolis extract, AuNPs, Fe<sub>3</sub>O<sub>4</sub> NPs and Au@Fe<sub>3</sub>O<sub>4</sub> BNPs are shown in Fig. 3a. The propolis extract exhibits a distinct peak at 3312 cm<sup>-1</sup>, attributed to the phenolic hydroxyl group. Meanwhile, other noticeable peaks at 2923, 2852, 1705, 1603, 1448, 1353, 1157, 1071 and 814, 767, 687 cm<sup>-1</sup> (Fig. 3b) can be related to the C–H bond stretching, asymmetrical stretches of CH<sub>2</sub>, C=O stretching, C=C stretching, aromatic C–H, O–H bending, aromatic C–O bond stretching, stretching of C–O functional groups and C–H bending in the phenolic rings, respectively (Matar and Andac 2023). Along with the mentioned components, those can be derived from the secondary metabolites of the extract, in which polyphenols may facilitate the formation of NPs and prevent agglomeration. In the FTIR spectrum of Fe<sub>3</sub>O<sub>4</sub> NPs, two distinct peaks at 3328 and 547 cm<sup>-1</sup> are observed, associated with the characteristic vibrations of O–H and Fe–O, confirming the synthesis of Fe<sub>3</sub>O<sub>4</sub> NPs (Desai et al. 2023). Additionally, the FTIR spectrum of Fe<sub>3</sub>O<sub>4</sub> NPs displays narrow peaks at 1577, 1349, 1167, and 1097 cm<sup>-1</sup>, which can be attributed to the C=C stretching, O–H bending, aromatic C–O bond stretching, and stretching of C–O functional groups present in flavonoid compounds involved in biogenic synthesis. The FTIR spectrum of AuNPs exhibits characteristic peaks at 3215, 2922, 2851, 1706, 1608, 1447, and 1351 cm<sup>-1</sup>, corresponding to O–H stretching, C–H bond stretching, asymmetrical stretches of CH<sub>2</sub>, C=O stretching, C=C stretching, aromatic C–H, and O–H bending. Furthermore, the FTIR spectrum of AuNPs shows sharp peaks at 1156, 1030, and 821, 767, 696 cm<sup>-1</sup>, which can be attributed to the aromatic C–O bond stretching, stretching of C–O functional groups, and C–H bending in the phenolic rings present in flavonoid and phenolic compounds, which likely act as reducing or capping agents during the green synthesis. Similarly, in the FTIR spectrum of Au@Fe<sub>3</sub>O<sub>4</sub> BNPs, the presence of a peak at 558 cm<sup>-1</sup> indicates Fe–O bonding. The FTIR spectrum of Au@Fe<sub>3</sub>O<sub>4</sub> BNPs exhibits peaks similar to the AuNPs spectra, with slight shifts in the distinct peaks to 3282, 2923, 2852, 1716, 1632, 1448, 1451, 1352, 1158, 1031, and 834, 768, 696 cm<sup>-1</sup>. These shifts are attributed to the biomolecules and functional groups responsible for attaching AuNPs to Fe<sub>3</sub>O<sub>4</sub> NPs, thereby reducing and stabilizing them.

## XRD studies

The XRD pattern was utilized to examine the crystalline nature and size of the AuNPs, Fe<sub>3</sub>O<sub>4</sub> NPs and Au@Fe<sub>3</sub>O<sub>4</sub> BNPs. In Fig. 3c, the XRD pattern reveals strong and intense peaks with no additional impurity crystalline phases, indicating the high crystallinity of these NPs. For AuNPs, Bragg's reflections were observed at 2θ angles of 38.14°, 44.41°,

64.67°, and 77.43°, corresponding to the (111), (200), (220), and (311) crystal planes, respectively. This pattern is consistent with PDF card no. 00-004-0784, confirming the presence of AuNPs. In the XRD pattern of Fe<sub>3</sub>O<sub>4</sub> NPs, Bragg's reflections at 2θ angles of 30.41°, 35.49°, 43.41°, 54.01°, 57.18°, and 62.88° corresponded to the (220), (311), (400), (422), (511), and (440) crystal planes, respectively. This pattern is consistent with PDF card no. 01-080-6403, confirming the presence of Fe<sub>3</sub>O<sub>4</sub> NPs. Upon analyzing the XRD pattern of Au@Fe<sub>3</sub>O<sub>4</sub> BNPs, reflections were found at 2θ angles of 30.16°, 35.57°, 38.15°, 43.24°, 44.37°, 53.77°, 57.22°, 62.78°, 64.58°, and 77.42°, corresponding to Fe (220), Fe (220), Au (111), Fe (400), Au (200), Fe (422), Fe (511), Fe (440), Au (220), and Au (311) crystal planes, respectively. The XRD pattern of Au@Fe<sub>3</sub>O<sub>4</sub> BNPs was similar to both patterns of AuNPs and Fe<sub>3</sub>O<sub>4</sub> NPs, indicating the formation of Au@Fe<sub>3</sub>O<sub>4</sub> BNPs.

Furthermore, the average crystallite size of the NPs was estimated using the Debye-Scherrer (D-S) equation, Williamson-Hall (W-H) method, and Halder-Wagner (H-W) method as described in Equations (3-5) (Nath et al. 2020; Radoń et al. 2023):

$$D = \frac{K\lambda}{\beta \cos\theta} \quad (3)$$

$$\beta \cos\theta = \frac{K\lambda}{D_{XRD}} + 4\epsilon \sin\theta \quad (4)$$

$$\left(\frac{FWHM}{\tan\theta}\right)^2 = \frac{K\lambda}{D_{XRD}} \frac{FWHM}{\tan\theta \sin\theta} + \left(\frac{\epsilon}{2}\right)^2 \quad (5)$$

where D is the crystallite size (nm), K is the Scherrer constant (0.94 for spherical crystallites), λ is the X-ray wavelength (0.154 nm), β (FWHM) is the full width of half-maximum signal, and θ is the Bragg's angle. Accordingly, the average crystallite size of the AuNPs, Fe<sub>3</sub>O<sub>4</sub> NPs, and Au@Fe<sub>3</sub>O<sub>4</sub> BNPs calculated to be 8.59, 11.66, and 14.28 nm, respectively (Table S1).

Also, the average crystallite size of the NPs was determined using the W-H method by plotting β cosθ against 4 sinθ and fitting a straight line to the data. In Fig. S2a, b, and e, the slope of the line represents the strain (ε), and the y-intercept provides the crystallite size. The average crystallite size of the AuNPs, Fe<sub>3</sub>O<sub>4</sub> NPs, and Au@Fe<sub>3</sub>O<sub>4</sub> BNPs, calculated from the W-H plot, was 6.8, 12.9, and 10.7 nm, respectively (Table S2).

Similarly, the H-W method was used to determine the average crystallite size of the NPs by plotting  $\left(\frac{FWHM}{\tan\theta}\right)^2$  against  $\frac{FWHM}{\tan\theta \sin\theta}$  (Fig. S2c, d, and f). The average crystallite size of the AuNPs, Fe<sub>3</sub>O<sub>4</sub> NPs, and Au@Fe<sub>3</sub>O<sub>4</sub> BNPs calculated from the H-W plot, was determined to be 6.7, 12.4, and

11.2 nm, respectively (Table S3). It's noteworthy that the crystallite sizes obtained from both the W-H method and the H-W method are quite similar and also close to that of the S-D equation.

## Magnetic properties

The magnetic characteristics of biosynthesized  $\text{Fe}_3\text{O}_4$  NPs and  $\text{Au@Fe}_3\text{O}_4$  BNPs were assessed using a vibrating sample magnetometer (VSM). In Fig. 3d, it is demonstrated that the  $\text{Au@Fe}_3\text{O}_4$  BNPs prepared in this study possess magnetic properties primarily attributed to the presence of  $\text{Fe}_3\text{O}_4$  NPs. To verify their magnetic characteristics, we conducted measurements of hysteresis loops at a temperature of 25 °C with an applied magnetic field ranging from -6000 to +6000 Oe. The saturation magnetization (Ms), coercivity (Hc), and saturation remanence (Mr) parameters of  $\text{Fe}_3\text{O}_4$  NPs and  $\text{Au@Fe}_3\text{O}_4$  BNPs are listed in Table S4. The saturation magnetization (Ms) values for  $\text{Fe}_3\text{O}_4$  NPs and  $\text{Au@Fe}_3\text{O}_4$  BNPs were found to be 57.22 and 30.99 emu/g, respectively, confirming the supermagnetic nature of both  $\text{Fe}_3\text{O}_4$  NPs and  $\text{Au@Fe}_3\text{O}_4$  BNPs. The slight decrease in the Ms of  $\text{Au@Fe}_3\text{O}_4$  BNPs can be attributed to the presence of Au on the outer surface of the  $\text{Fe}_3\text{O}_4$  NPs. This outcome highlights the outstanding magnetic properties of these NPs in comparison to other magnetic NPs (Desai et al. 2023). Due to their impressive magnetic response, these biosynthesized  $\text{Fe}_3\text{O}_4$  NPs and  $\text{Au@Fe}_3\text{O}_4$  BNPs hold promise for diverse biomedical and environmental applications. In terms of environmental applications, the magnetic properties of the NPs contribute to an increased surface area available for adsorption. This phenomenon is crucial for enhancing the adsorption capacity of the NPs, making them more effective than their non-magnetic counterparts in removing dye molecules from aqueous solutions. Additionally, the magnetic properties of the NPs play a crucial role in their performance in antioxidant applications. The ability to guide and target these NPs using a magnetic field allows for the precise delivery of antioxidants to specific sites within biological systems, thereby preserving their stability and biocompatibility. This targeted approach enhances the therapeutic potential of the NPs in mitigating oxidative stress and related disorders (Moskvin et al. 2021).

## FE-SEM, HRTEM with SAED analysis and Zeta potential

The morphology and particle size of  $\text{Fe}_3\text{O}_4$  NPs and  $\text{Au@Fe}_3\text{O}_4$  BNPs were examined using FE-SEM and TEM (Fig. 4 and Fig. 5). Fig. 4a-c and Fig. 5a-c display FE-SEM and TEM images of  $\text{Fe}_3\text{O}_4$  NPs and  $\text{Au@Fe}_3\text{O}_4$  BNPs at different magnifications. These images show that the synthesized  $\text{Fe}_3\text{O}_4$  NPs had uniform and monodispersive spherical

shapes of varying sizes. In contrast, the  $\text{Au@Fe}_3\text{O}_4$  BNPs appeared aggregated with spherical, rectangular shapes, and slightly larger sizes. This uniform dispersion of particles may be attributed to the presence of bio-analytes on the particle surface, which acted as stabilizing agents. The analysis of the TEM micrograph showed that the biosynthesized  $\text{Fe}_3\text{O}_4$  NPs and  $\text{Au@Fe}_3\text{O}_4$  BNPs had an average size of  $5.45 \pm 1.28$  nm and  $15.67 \pm 4.02$  nm, respectively, as shown in the size distribution histogram (Fig. 4d and Fig. 5d). In Fig. 4e and Fig. 5e, HRTEM images at 2 nm show fine fringes within the  $\text{Fe}_3\text{O}_4$  NPs and  $\text{Au@Fe}_3\text{O}_4$  BNPs. Fig. 5e also depicts the homogeneous presence of  $\text{Fe}_3\text{O}_4$  NPs and AuNPs in the HRTEM image of  $\text{Au@Fe}_3\text{O}_4$  BNPs, as confirmed through EDX analysis.

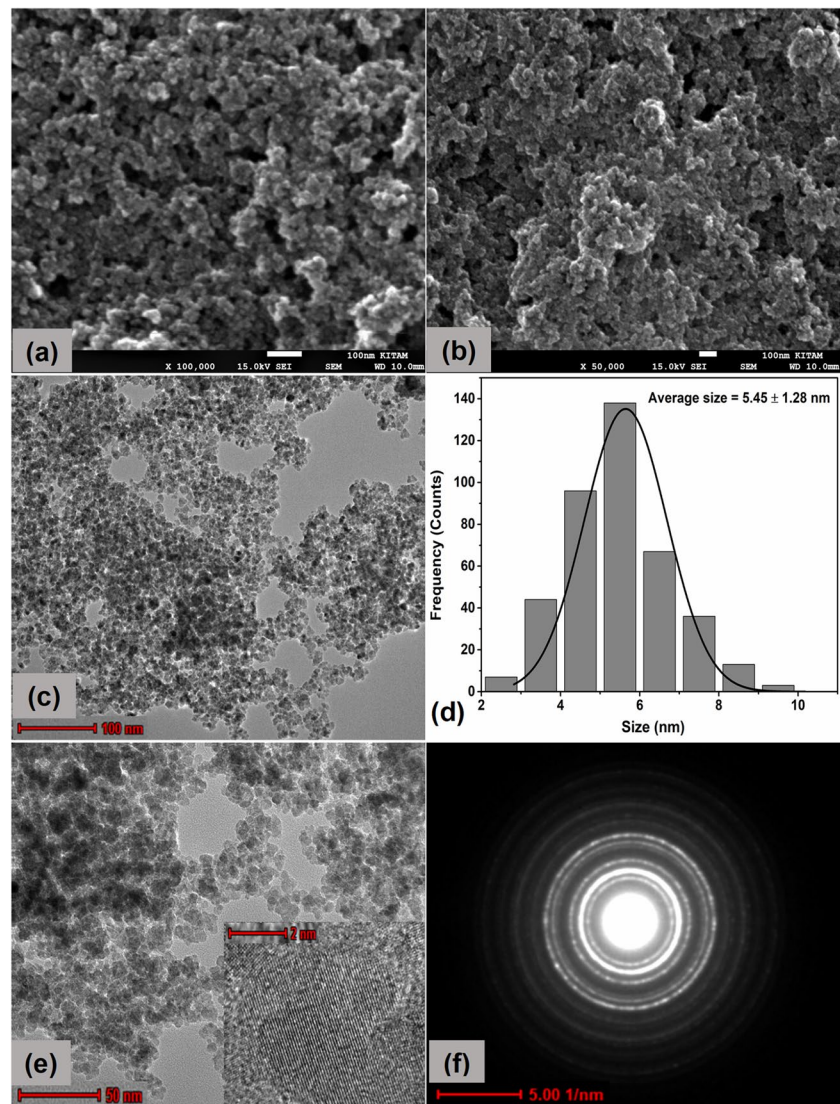
Furthermore, SAED patterns were utilized to examine the crystalline nature of the synthesized  $\text{Fe}_3\text{O}_4$  NPs and  $\text{Au@Fe}_3\text{O}_4$  BNPs (Fig. 4f) and (Fig. 5f). The d-spacing of  $\text{Fe}_3\text{O}_4$  NPs and  $\text{Au@Fe}_3\text{O}_4$  BNPs was calculated through SAED patterns using Image J software (Table S5). The SAED patterns of the  $\text{Fe}_3\text{O}_4$  NPs and  $\text{Au@Fe}_3\text{O}_4$  BNPs indicated the presence of intense bright spots on the diffraction rings, confirming the polycrystalline nature of these NPs. The diffraction rings of  $\text{Fe}_3\text{O}_4$  BNPs were found at interplanar distances of 0.293, 0.252, 0.205, 0.169, 0.160, and 0.146 nm, corresponding to the (220), (311), (400), (422), (511), and (440) planes of  $\text{Fe}_3\text{O}_4$ . Whereas the SAED pattern of  $\text{Au@Fe}_3\text{O}_4$  BNPs in Fig. 6f clearly depicts diffraction spots corresponding to the (220), (311), (400), (422), (511), and (440) planes of  $\text{Fe}_3\text{O}_4$ , and the planes (111), (200), (220), and (311) were observed for Au. Thus, the measurements obtained from the SAED pattern very closely align with the measurements of XRD analysis.

The zeta potential of the  $\text{Fe}_3\text{O}_4$  NPs and  $\text{Au@Fe}_3\text{O}_4$  NPs showed a negative charge, -26.3 mV and -34.7 mV, respectively (Fig. S3). The notable negative zeta potential observed in  $\text{Fe}_3\text{O}_4$  NPs and  $\text{Au@Fe}_3\text{O}_4$  NPs is associated with their prolonged stability and colloidal structure. This negative charge plays a crucial role in preventing the agglomeration of nanoparticles in the solution by fostering repulsion among them. Since the  $\text{Fe}_3\text{O}_4$  NPs and  $\text{Au@Fe}_3\text{O}_4$  NPs have a negative charge, they are likely to attract and interact with cationic dyes. In this case, cationic dyes such as MB, CV, and MG dye, which carry a positive charge, would be attracted to the negatively charged surface of these nanoparticles. This electrostatic interaction between the negatively charged nanoparticles and the positively charged cationic dyes can lead to adsorption of the dyes onto the nanoparticle surface.

## EDX analysis

The elemental compositions of  $\text{Fe}_3\text{O}_4$  NPs and  $\text{Au@Fe}_3\text{O}_4$  BNPs were determined by EDX as shown in Fig. 6a, b. In Fig. 6a, the EDX spectrum of the  $\text{Fe}_3\text{O}_4$  NPs indicates the

**Fig. 4** FESEM images at (a) 100 nm and at (b) 50 nm scale, TEM micrographs at (c) 100 nm scale, (d) particle size distribution, (e) HR-TEM image at 50 nm and showing fringe spacing at 2 nm scale, and (f) SAED pattern of biosynthesized  $\text{Fe}_3\text{O}_4$  NPs



predominant presence of carbon (C, 54.3 wt%), oxygen (O, 23.1 wt%), and iron (Fe, 22.6 wt%) within the NPs, confirming the successful synthesis of  $\text{Fe}_3\text{O}_4$  NPs. In Fig. 6b, the EDX spectra reveal the presence of elemental carbon (C, 21.4 wt%), oxygen (O, 17.3 wt%), and iron (Fe, 53.9 wt%) along with gold (Au, 7.5 wt%) peaks, confirming the successful synthesis of  $\text{Au@Fe}_3\text{O}_4$  BNPs.

Additionally, the EDX spectra of NPs indicate the presence of carbon and oxygen elements, attributed to extract role as the reducing agent in the biosynthesis process. In the mapping spectrum, the red, yellow, blue, and purple dots represent the distribution of C, O, Fe and Au elements within the NPs.

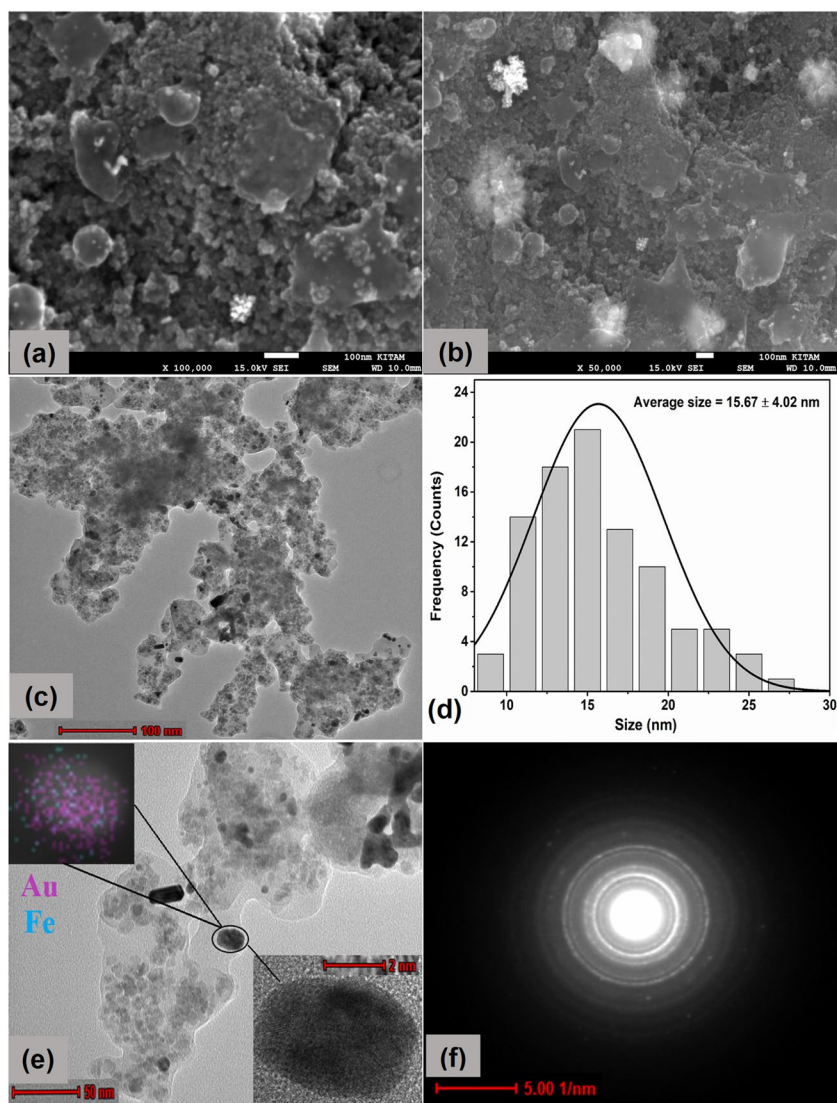
### XPS analysis

XPS was used to investigate the oxidation state and chemical composition of the  $\text{Fe}_3\text{O}_4$  NPs and  $\text{Au@Fe}_3\text{O}_4$  BNPs.

Table S6 presents comprehensive data regarding the elemental composition obtained through XPS analysis. Fig. S4 and Fig. 7 show the XPS data for  $\text{Fe}_3\text{O}_4$  NPs and  $\text{Au@Fe}_3\text{O}_4$  BNPs. Fig. S4a presents the survey scan of the  $\text{Fe}_3\text{O}_4$  NPs, confirming the presence of C, O, and Fe in these NPs, which is consistent with the results of the EDX analysis. The Fig. S4c and Fig. 7c show the C 1s spectra of  $\text{Fe}_3\text{O}_4$  NPs. As observed, C 1s spectra can be deconvoluted into three peaks at 284.6, 286.2, and 288.5 eV, corresponding to (C-C, C-H), C-O, and C=O, respectively (Ravelo-Nieto et al. 2023). In Fig. S4d and Fig. 7d, the O 1s spectra can be deconvoluted into two peaks located at 530.1 and 531.0 eV, corresponding to the oxygen species in the Fe-O component of magnetite and oxygen in the C-O or O-H components (López et al. 2023). The presence of carbon and oxygen in the  $\text{Fe}_3\text{O}_4$  NPs was attributed to the capping of propolis extract biomolecules. Furthermore, Fig. S4b and Fig. 7b display the narrow scan of the Fe 2p spectrum, confirming the presence of



**Fig. 5** FESEM images at (a) 100 nm and at (b) 50 nm scale, TEM micrographs at (c) 100 nm scale, (d) particle size distribution, (e) HR-TEM image at 50 nm and showing fringe spacing at 2 nm scale, and (f) SAED pattern of biosynthesized Au@Fe<sub>3</sub>O<sub>4</sub> BNPs



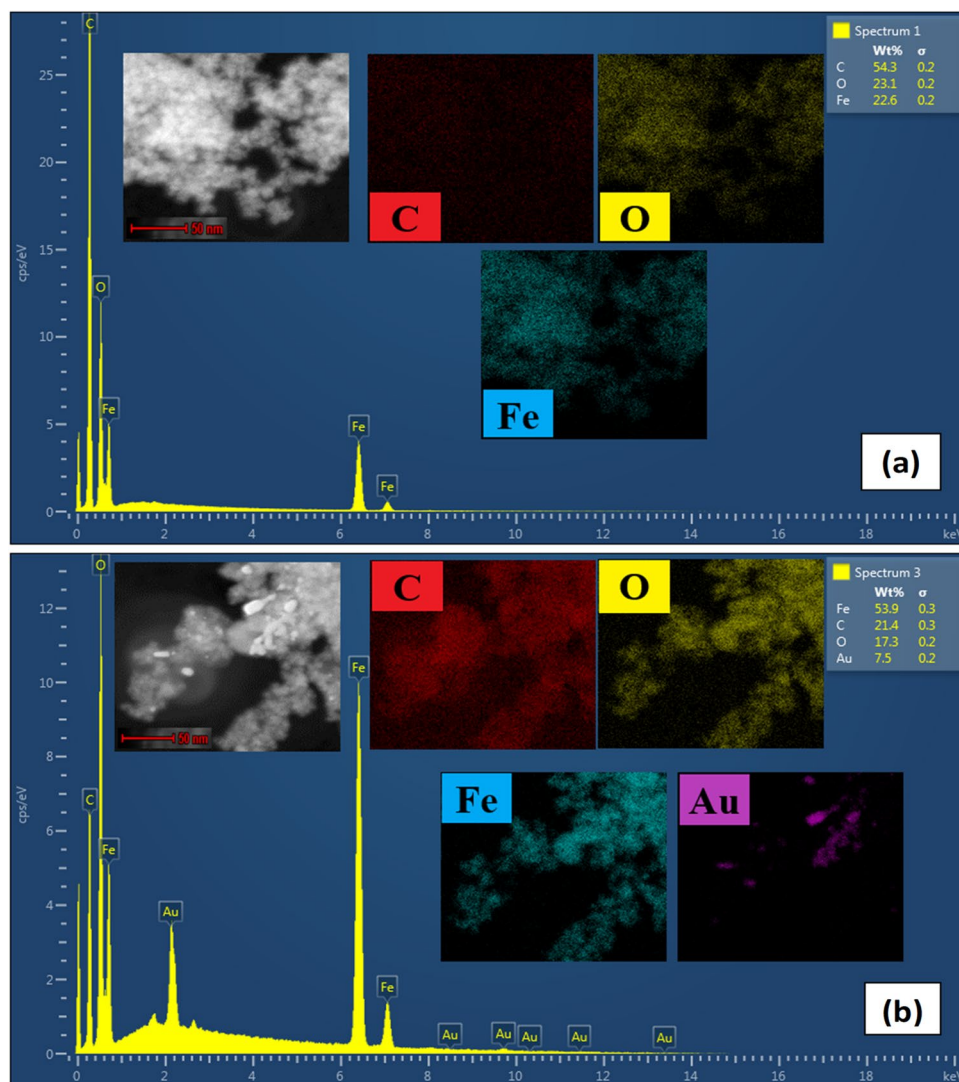
characteristic peaks such as Fe2p<sub>3/2</sub> (710.7 eV) and Fe2p<sub>1/2</sub> (724.4 eV) in the NPs. These peaks can be further subdivided into six peaks at 710.1, 711.2, 713.7, 723.2, 724.6, and 727.2 eV. The peaks at 710.1, 711.2, 723.2, and 724.6 eV indicate the presence of Fe-O bonds in the Fe<sup>2+</sup> ion, while the peaks at 713.7 and 727.2 eV were associated with Fe-O bonds in the Fe<sup>3+</sup> ion within the Fe<sub>3</sub>O<sub>4</sub> (Rajan et al. 2020). In Fig. 7a, the XPS survey spectrum of Au@Fe<sub>3</sub>O<sub>4</sub> BNPs confirms the presence of C, O, Fe, and Au, which is consistent with the results of the EDX analysis. Notably, the intensity of the C 1s peak increased while the O 1s peak decreased noticeably. This change was due to the presence of Au on the outer surface of the Fe<sub>3</sub>O<sub>4</sub> NPs (Fe<sub>3</sub>O<sub>4</sub> NPs coated with Au). Fig. 7e shows the Au 4f spectra of Au@Fe<sub>3</sub>O<sub>4</sub> BNPs. As observed, the Au 4f spectra can be deconvoluted into two doublet peaks at 84.1 and 87.8 eV, corresponding to Au 4f<sub>7/2</sub> and Au 4f<sub>5/2</sub>, respectively (Naraginti and Li 2017). Moreover, there was almost no difference between the positions of

the peaks in the C 1s and Fe 2p spectra for both Fe<sub>3</sub>O<sub>4</sub> NPs and Au@Fe<sub>3</sub>O<sub>4</sub> BNPs. Meanwhile, the peak intensity of the O 1s for Au@Fe<sub>3</sub>O<sub>4</sub> BNPs decreased significantly, indicating that more AuNPs were coated on the surface of Fe<sub>3</sub>O<sub>4</sub> NPs, as well as highlighting the strong interaction between AuNPs and Fe<sub>3</sub>O<sub>4</sub>. Taken together, these results confirm the successful fabrication of Au@Fe<sub>3</sub>O<sub>4</sub> BNPs.

### Evaluation of photocatalytic performance

In this section, we assessed the photocatalytic performance of Fe<sub>3</sub>O<sub>4</sub> NPs and Au@Fe<sub>3</sub>O<sub>4</sub> BNPs as nanocatalysts by investigating their ability to degrade the dyes MB, CV, and MG, which are considered as toxic pollutants. After adding Fe<sub>3</sub>O<sub>4</sub> NPs and Au@Fe<sub>3</sub>O<sub>4</sub> BNPs to the dye solution and exposing it to fluorescent lamp light, we recorded the photocatalytic results of MB, CV, and MG dyes at regular time intervals using Fe<sub>3</sub>O<sub>4</sub> NPs and Au@Fe<sub>3</sub>O<sub>4</sub> BNPs. Over time,

**Fig. 6** EDX spectrum and mapping images of (a) biosynthesized  $\text{Fe}_3\text{O}_4$  NPs and (b)  $\text{Au}@ \text{Fe}_3\text{O}_4$  BNPs



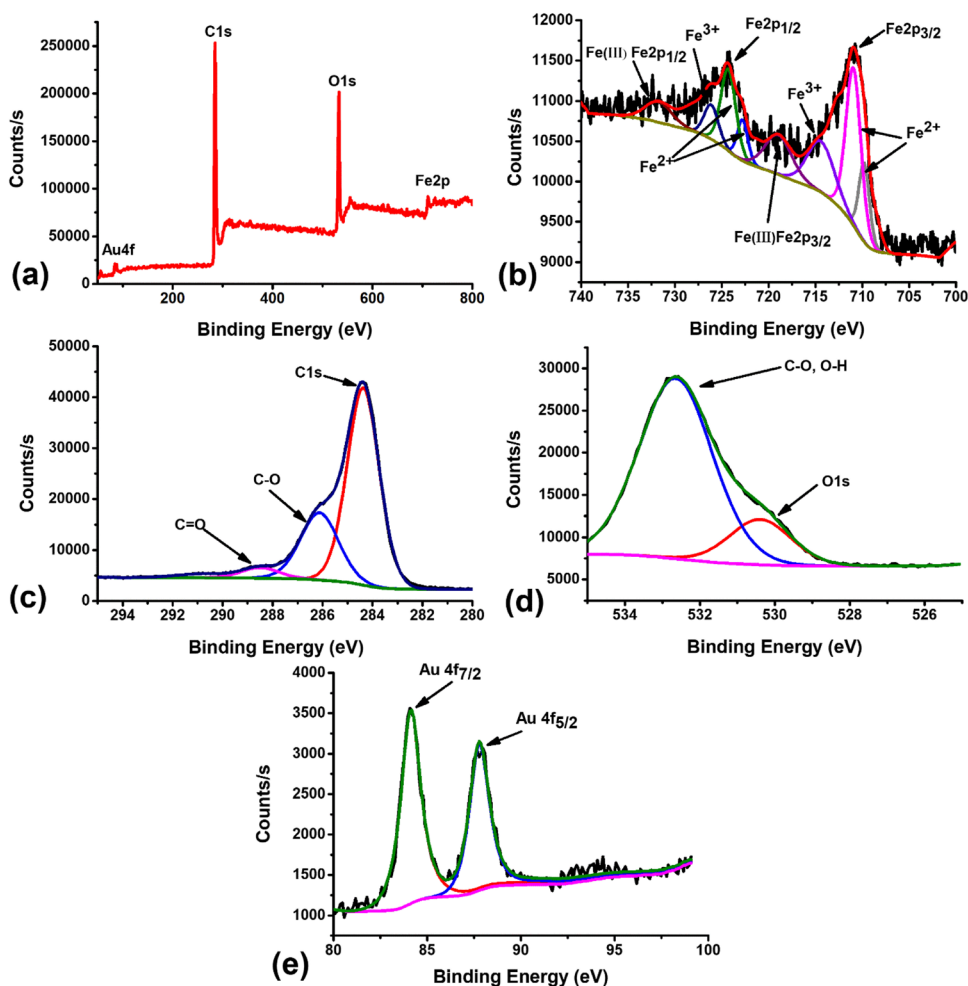
we observed changes in the absorption spectra of MB, CV, and MG, with characteristic absorption wavelengths ( $\lambda_{\text{max}}$ ) at 665 nm, 580 nm, and 618 nm, respectively. The absorption peaks of these dyes decreased with time, further supported by the fading of the dye color, as shown in the insets of Fig. S5 and Fig. S6.

#### Degradation of MB, CV, and MG dyes using $\text{Fe}_3\text{O}_4$ NPs

The photocatalytic performance of biosynthesized  $\text{Fe}_3\text{O}_4$  NPs to degrade MB, CV and MG dyes was examined under fluorescent lamp light at room temperature. Fig. 8 represents UV-visible absorption plots of photodegradation of MB, CV, and MG dye treated with  $\text{Fe}_3\text{O}_4$  NPs at different time intervals and their degradation percentages. Increasing the contact time resulted in a higher percentage of dye removal for all dyes examined. The ideal contact times for removing MB, CV, and MG were determined to be 70 min, 50 min, and 60 min, respectively, leading to the highest levels of dye

removal (Fig. 8a, b, c). As displayed in Fig. 8d, e, f,  $\text{Fe}_3\text{O}_4$  NPs degraded the MB, CV, and MG dye at a concentration of 10 ppm with 95.2%, 99.4%, and 96.2% degradation efficiency, respectively. Meanwhile, the removal of MB, CV, and MG dyes using  $\text{Fe}_3\text{O}_4$  NPs was performed in the dark for 70 min, 50 min, and 60 min, respectively, as shown in Fig. S7. Still, the removal percentage efficiency was relatively lesser compared to the degradation efficiency of MB, CV, and MG dye in the presence of light (Table S7). The removal efficiency time for the dark reaction was 20 h for MB, CV, and MG dyes, whereas the degradation efficiency time for the light reaction was 70 min, 50 min, and 60 min for MB, CV, and MG dyes, respectively. It is well known that MB, CV, and MG act as cationic dyes in the aqueous solution. The presence of certain forces, such as hydrogen bonding, electrostatic interactions and hydrophobic-hydrophobic interactions, plays a crucial role in regulating the attachment of MB, CV, and MG dye (Cheng et al. 2023). Synthesized  $\text{Fe}_3\text{O}_4$  NPs were produced using propolis

**Fig. 7** (a) XPS survey spectrum of Au@Fe<sub>3</sub>O<sub>4</sub> BNPs, (b) Fe2p spectra, (c) C 1s spectra, (d) O 1s spectra, and Au 4f spectra



extract containing bioactive compounds such as flavonoids and phenolic compounds. Analysis of FTIR and XPS spectra revealed the presence of functional groups such as hydroxyl groups (–OH) and carbonyl groups (C=O) on the surface of Fe<sub>3</sub>O<sub>4</sub> NPs. These functional groups can potentially interact with the functional groups of dyes (MB, CV, MG) through hydrogen bonding (Fig. 10a). Additionally, hydrophobic-hydrophobic interactions may form due to the hydrophobic surface of the Fe<sub>3</sub>O<sub>4</sub> NPs, which facilitates increased interactions between the Fe<sub>3</sub>O<sub>4</sub> NPs and (MB, CV, MG) dyes in an aqueous medium (Fig. 10a). Furthermore, the high surface area and high negative surface charge of the Fe<sub>3</sub>O<sub>4</sub> NPs facilitate the physisorption of these dyes onto the Fe<sub>3</sub>O<sub>4</sub> NPs, as well as increased electrostatic interaction between the Fe<sub>3</sub>O<sub>4</sub> NPs and the dye (Fig. 10a).

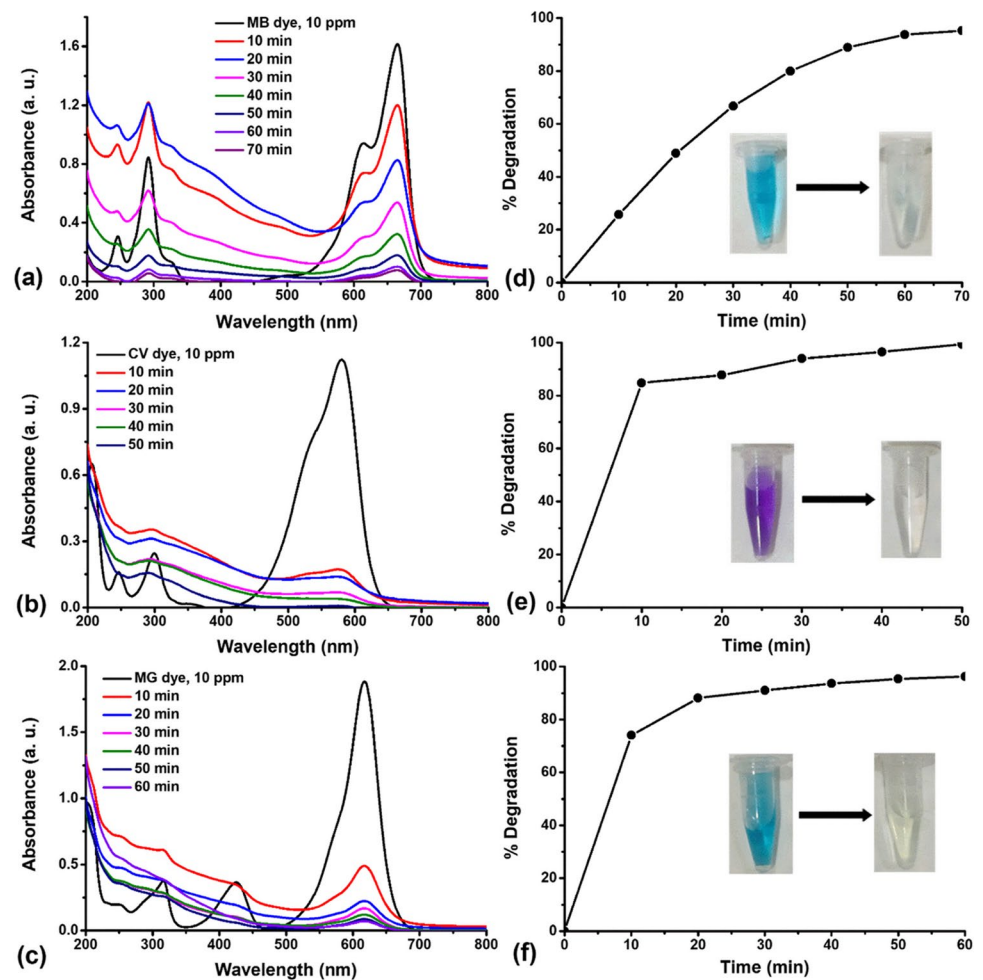
#### Degradation of MB, CV, and MG dyes using Au@Fe<sub>3</sub>O<sub>4</sub> BNPs

High efficiency was observed in the removal of textile-toxic basic dyes (MB, CV, and MG dye) using biosynthesized Au@Fe<sub>3</sub>O<sub>4</sub> BNPs as nanocatalyst at room temperature, without the addition of any catalyst. Figure 9 represents

UV-visible absorption plots of photocatalytic degradation of MB, CV, and MG dye treated with Au@Fe<sub>3</sub>O<sub>4</sub> BNPs at different time intervals and their degradation percentages. Increasing the contact time resulted in a higher percentage of dye removal for all dyes examined. The ideal contact times for removing MB, CV, and MG were determined to be 50 min, 30 min, and 50 min, respectively, leading to the highest levels of dye removal (Fig. 9a, b, c). As displayed in Fig. 9d, e, f, Au@Fe<sub>3</sub>O<sub>4</sub> BNPs degraded the MB, CV and MG dye at a concentration of 10 ppm with 97.1%, 99.1%, and 98.1% degradation efficiency, respectively. Meanwhile, the removal of MB, CV, and MG dyes using Au@Fe<sub>3</sub>O<sub>4</sub> NPs was performed in the dark for 50 min, 30 min, and 50 min, respectively, as shown in Fig. S8. Still, the removal percentage efficiency was relatively lesser compared to the degradation efficiency of MB, CV, and MG dye in the presence of light (Table S7). The removal efficiency time for the dark reaction was 20 h for MB, CV, and MG dyes, whereas the degradation efficiency time for the light reaction was 50 min, 30 min, and 50 min for MB, CV, and MG dyes, respectively. This improvement in dye removal percentage with extended contact time can be attributed to the stronger



**Fig. 8** Absorption spectra of photocatalytic degradation of (a) MB, (b) CV, and (c) MG dye treated with  $\text{Fe}_3\text{O}_4$  NPs at different time points and removal efficiency percentages of (d) MB, (e) CV, and (f) MG dye



attraction between dye molecules and the active sites on the adsorbent molecules. The effectiveness of  $\text{Au}@Fe_3O_4$  BNPs synthesized through the green method can be attributed to the presence of elemental gold and biomolecule compounds from propolis extract, forming a coating on the  $\text{Fe}_3\text{O}_4$  NPs surface. Furthermore, the core-shell structure and the larger surface area of these NPs contribute significantly to their high adsorption capacity for cationic dyes (Das et al. 2023). It appears that the functional groups on the nanoparticle surface play a crucial role in the adsorption process, as indicated by FTIR and XPS analysis. These functional groups can potentially interact with the functional groups of dyes (MB, CV, MG) through hydrogen bonding. These functional groups can potentially interact with the functional groups of dyes (MB, CV, MG) through the presence of certain forces, such as hydrogen bonding, electrostatic interactions, and hydrophobic-hydrophobic interactions (Fig. 10b). There is no significant difference between the adsorption capacities of  $\text{Fe}_3\text{O}_4$  and  $\text{Au}@Fe_3O_4$  in the degradation of those dyes. In summary, the results demonstrate that biosynthesized  $\text{Fe}_3\text{O}_4$  NPs and  $\text{Au}@Fe_3O_4$  BNPs are effective in adsorbing basic dyes with cationic charged surfaces. Table S8 shows

a comparative table of the photocatalytic activity of  $\text{Fe}_3\text{O}_4$  NPs and  $\text{Au}@Fe_3O_4$  BNPs with some reported materials.

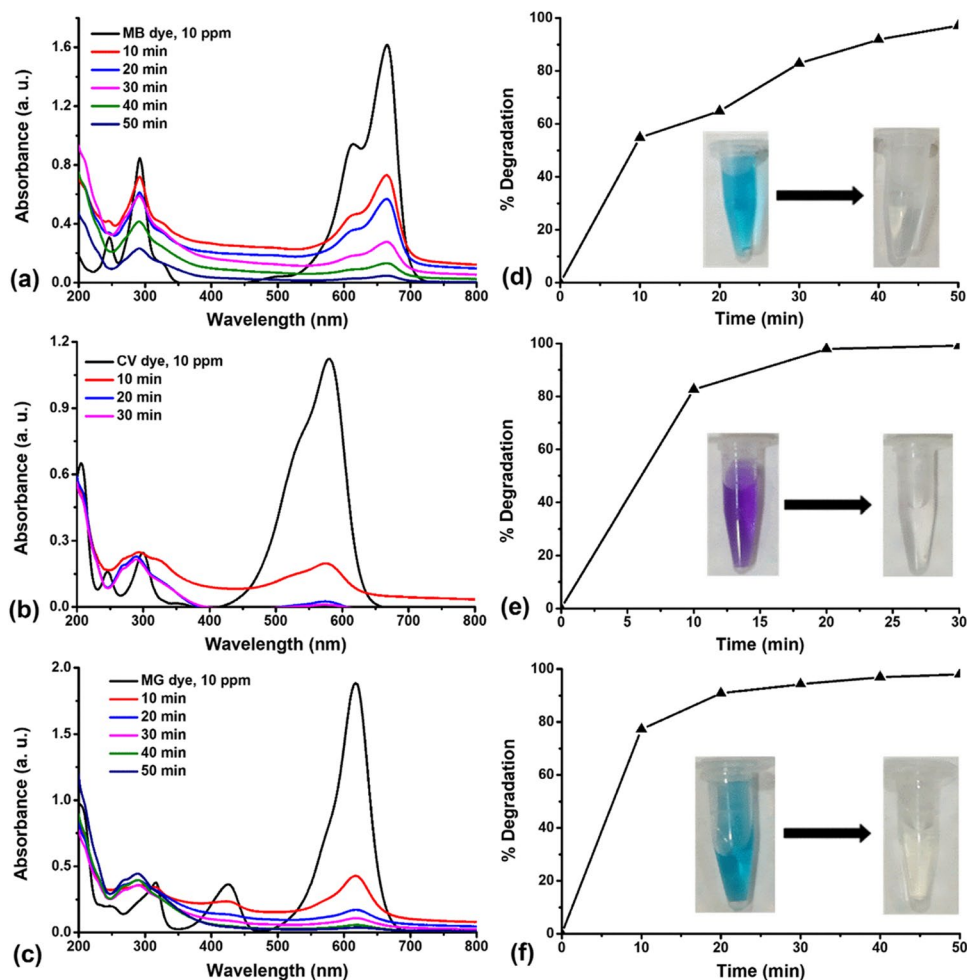
To check the reusability of  $\text{Au}@Fe_3O_4$  NPs, FTIR analysis was conducted for both fresh and regenerated  $\text{Au}@Fe_3O_4$  NPs. The desorption of the synthesized NPs involved washing them three times with ethanol and subsequently drying them in the oven. According to the FTIR results depicted in Fig. S9, there were no significant changes in the nature of the nanoparticles, confirming the stability of the regenerated  $\text{Au}@Fe_3O_4$ . Therefore, these green synthesized stable nanoparticles can be effectively utilized for the removal of toxic dyes from aqueous solutions.

#### FTIR analysis of MB, CV, and MG after adsorption

After the MB, CV, and MG dye adsorption processes using  $\text{Fe}_3\text{O}_4$  NPs and  $\text{Au}@Fe_3O_4$  BNPs, the intensity of the peaks in the adsorbents shifted without any change in their positions (Fig. 11). This shift can be attributed to the interaction and binding of the MB, CV, and MG dyes with the adsorbent surface. In the FTIR spectrum of  $\text{Fe}_3\text{O}_4$  NPs-MB and  $\text{Au}@Fe_3O_4$  BNPs-MB, the peaks corresponding to the -OH,



**Fig. 9** Absorption spectra of photocatalytic degradation of (a) MB, (b) CV, and (c) MG dye treated with Au@Fe<sub>3</sub>O<sub>4</sub> BNPs at different time points and degradation percentages of (d) MB, (e) CV, and (f) MG dye



C=O, C=C, and C-O-C functional groups shifted to lower wavelengths, indicating adsorptive interactions between these functional groups present on the surfaces of Fe<sub>3</sub>O<sub>4</sub> NPs and Au@Fe<sub>3</sub>O<sub>4</sub> BNPs with the MB dye (Matar and Andac 2023).

In the FTIR spectra of Fe<sub>3</sub>O<sub>4</sub> NPs-CV and Au@Fe<sub>3</sub>O<sub>4</sub> BNPs-CV, important sharp peaks appeared at 1584 cm<sup>-1</sup> and 1361 cm<sup>-1</sup> for Fe<sub>3</sub>O<sub>4</sub> NPs-CV, and at 1584 cm<sup>-1</sup> and 1360 cm<sup>-1</sup> for Au@Fe<sub>3</sub>O<sub>4</sub> BNPs-CV. These peaks are attributed to the C=C aromatic stretching vibration and C-N aromatic tertiary amine stretching vibration, respectively (Foroutan et al. 2021; Shalaby et al. 2021). Distinctive changes were observed in the FTIR spectrum of Fe<sub>3</sub>O<sub>4</sub> NPs-MG and Au@Fe<sub>3</sub>O<sub>4</sub> BNPs-MG. A new sharp peak at 1735 cm<sup>-1</sup> appeared in the FTIR spectrum of Fe<sub>3</sub>O<sub>4</sub> NPs-MB, corresponding to the C=O stretching vibration. The other peaks at 1583 cm<sup>-1</sup> and 1365 cm<sup>-1</sup> are associated with C=C stretching in the benzene rings and C-N stretching vibration, respectively. Similarly, in the FTIR Spectrum of Au@Fe<sub>3</sub>O<sub>4</sub> BNPs-MG, the peaks of the -OH, C=O, C=C, and C-O-C functional groups also shifted to lower wavelengths, along with the C-N stretching vibration (Zhang et al. 2022). These

observations confirm the adsorption interaction of the functional groups on the surfaces of Fe<sub>3</sub>O<sub>4</sub> NPs and Au@Fe<sub>3</sub>O<sub>4</sub> BNPs with MB, CV, and MG.

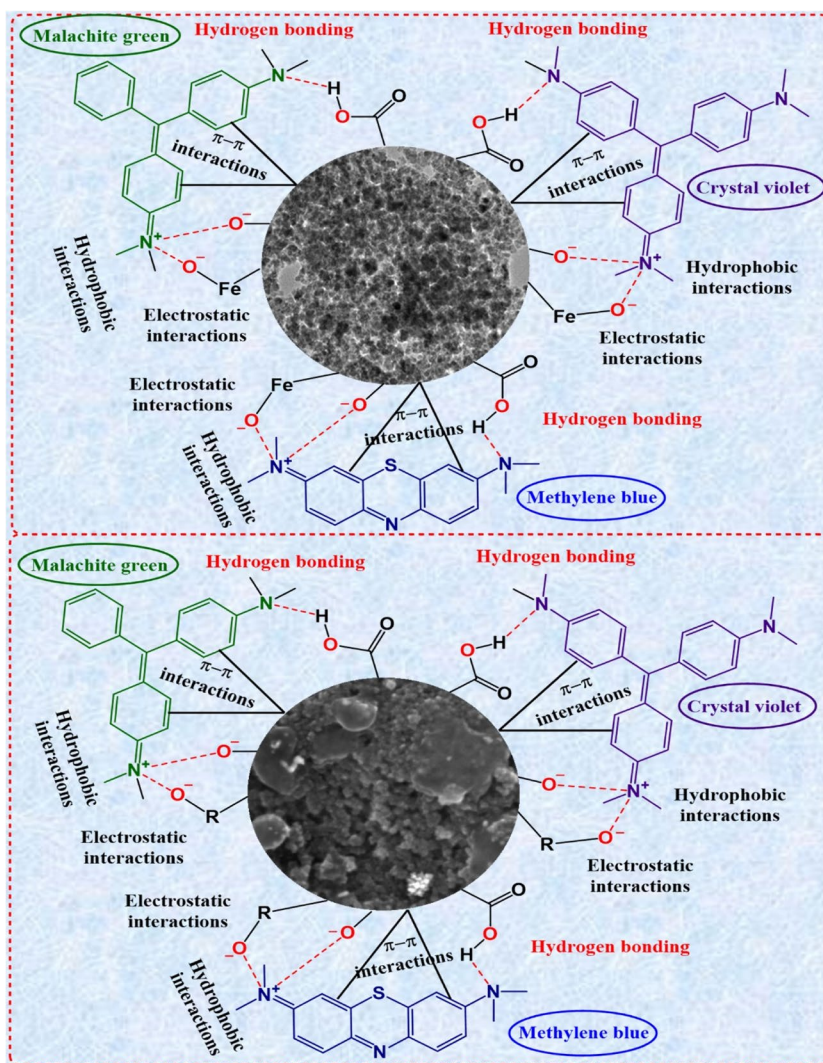
### Study of photodegradation kinetics

The Fe<sub>3</sub>O<sub>4</sub> NPs and Au@Fe<sub>3</sub>O<sub>4</sub> BNPs conducted kinetic investigations on the photodegradation of MB, CV, and MG dyes using the pseudo-first-order and pseudo-second-order models (Purkait et al. 2023). These models assist in determining the rate constants for the photodegradation of MB, CV, and MG dyes in the presence of Fe<sub>3</sub>O<sub>4</sub> NPs and Au@Fe<sub>3</sub>O<sub>4</sub> BNPs as photocatalysts, and the rate constants obtained were used to understand the mechanism of the reaction, as indicated by the following equations (6-7):

$$\ln A_t = -K_1 t + \ln A_0 \quad (6)$$

$$\frac{1}{A_t} = K_2 t + \frac{1}{A_0} \quad (7)$$

**Fig. 10** The adsorption mechanism of MB, CV, MG onto (a) Fe<sub>3</sub>O<sub>4</sub> NPs and (b) Au@Fe<sub>3</sub>O<sub>4</sub> NPs



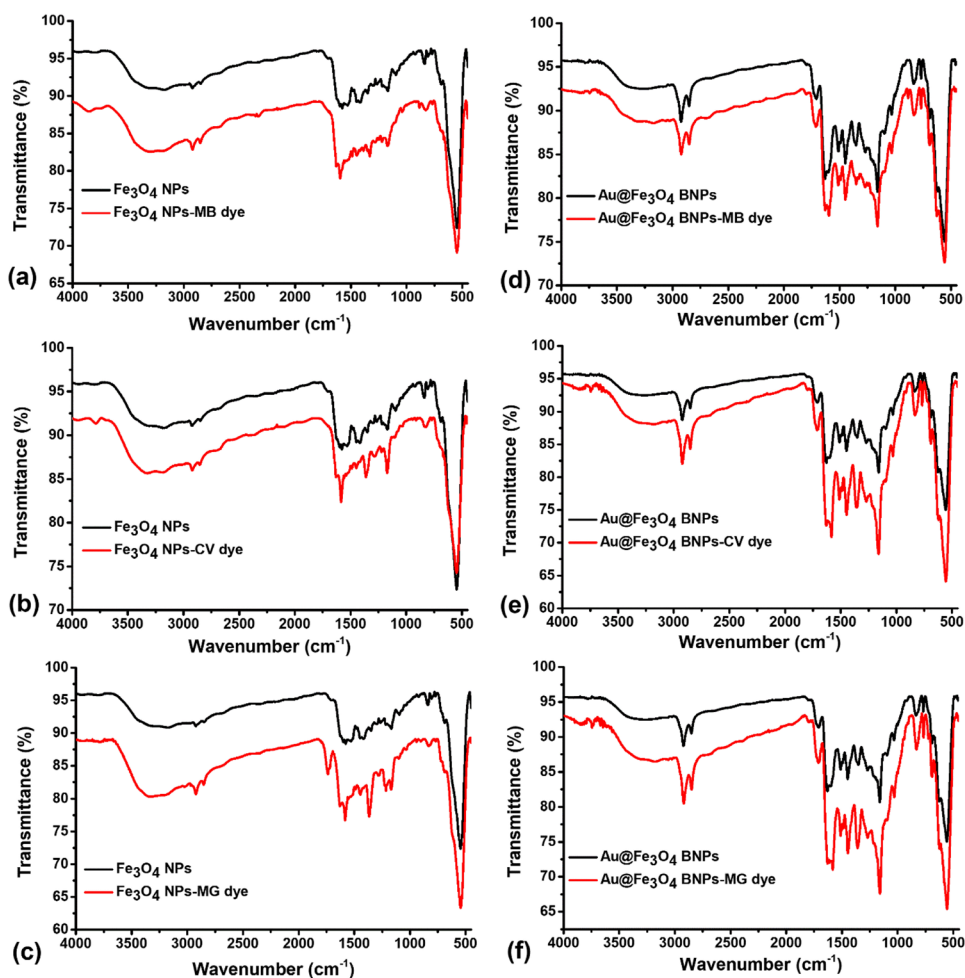
where  $K_1$  and  $K_2$  are the adsorption rate constants of the Langmuir-Hinshelwood model and the pseudo-second-order model. Once the suitable linear graphs for these models were plotted, we proceeded to compute the constant values, which are presented in Table 1.

Fig. 12 illustrates kinetic graphs representing both the pseudo-first-order model and pseudo-second-order kinetic models of MB-Fe<sub>3</sub>O<sub>4</sub> NPs, CV-Fe<sub>3</sub>O<sub>4</sub> NPs, and MG-Fe<sub>3</sub>O<sub>4</sub> NPs. Table 1 presents a summary of the correlation coefficient ( $R^2$ ) values and various rate constants. The pseudo-first-order kinetics values of  $K_1$  and  $R^2$  for the MB-Fe<sub>3</sub>O<sub>4</sub> NPs, CV-Fe<sub>3</sub>O<sub>4</sub> NPs, and MG-Fe<sub>3</sub>O<sub>4</sub> NPs are found to be (0.0430 min<sup>-1</sup> and 0.9938), (0.0969 min<sup>-1</sup> and 0.9730) and (0.0646 min<sup>-1</sup> and 0.9466), respectively. In the case of pseudo-second-order kinetics values of  $K_2$  and  $R^2$  for the MB-Fe<sub>3</sub>O<sub>4</sub> NPs, CV-Fe<sub>3</sub>O<sub>4</sub> NPs, and MG-Fe<sub>3</sub>O<sub>4</sub> NPs are found to be (0.1736 min<sup>-1</sup> and 0.8454), (2.2191 min<sup>-1</sup> and 0.5788) and (0.2263 min<sup>-1</sup> and 0.9867), respectively. It's evident that, in terms of contact time, the pseudo-first-order

kinetics proved to be the most favorable for degrading MB, CV, and MG using Fe<sub>3</sub>O<sub>4</sub> NPs. Their respective  $R^2$  values were notably high at 0.9908, 0.9336, and 0.8834, respectively.

Fig. 13 illustrates kinetic graphs representing both the pseudo-first-order model and pseudo-second-order kinetic models of MB-Au@Fe<sub>3</sub>O<sub>4</sub> BNPs, CV-Au@Fe<sub>3</sub>O<sub>4</sub> BNPs, and MG-Au@Fe<sub>3</sub>O<sub>4</sub> BNPs. Table 1 presents a summary of the correlation coefficient ( $R^2$ ) values and various rate constants. The pseudo-first-order kinetics values of  $K_1$  and  $R^2$  for the MB-Au@Fe<sub>3</sub>O<sub>4</sub> BNPs, CV-Au@Fe<sub>3</sub>O<sub>4</sub> BNPs, and MG-Au@Fe<sub>3</sub>O<sub>4</sub> BNPs are found to be (0.0652 min<sup>-1</sup> and 0.9892), (0.1686 min<sup>-1</sup> and 0.9886) and (0.0881 min<sup>-1</sup> and 0.9717), respectively. In the case of pseudo-second-order kinetics values of  $K_2$  and  $R^2$  for the MB-Au@Fe<sub>3</sub>O<sub>4</sub> BNPs, CV-Au@Fe<sub>3</sub>O<sub>4</sub> BNPs, and MG-Au@Fe<sub>3</sub>O<sub>4</sub> BNPs are found to be (0.3536 min<sup>-1</sup> and 0.7059), (3.3387 min<sup>-1</sup> and 0.8832) and (0.5187 min<sup>-1</sup> and 0.9192), respectively. It's evident that, in terms of contact time, the pseudo-first-order kinetics

**Fig. 11** FTIR spectra of  $\text{Fe}_3\text{O}_4$  NPs before adsorption of MB/CV/MG dyes, (a) after MB adsorption, (b) after CV adsorption, and (c) after MG adsorption; FTIR spectra of  $\text{Au}@Fe_3\text{O}_4$  BNPs before adsorption of MB/CV/MG dyes, (d) after MB adsorption, (e) after CV adsorption, and (f) after MG adsorption



**Table 1** Kinetics parameters associated with the photocatalytic degradation of MB, CV, and MG dye using  $\text{Fe}_3\text{O}_4$  NPs and  $\text{Au}@Fe_3\text{O}_4$  BNPs

Samples	First-order kinetic model		Second-order kinetic model		degradation (%)
	$K_1$ ( $\text{min}^{-1}$ )	$R^2$	$K_2$ ( $\text{L mg}^{-1} \text{min}^{-1}$ )	$R^2$	
MB- $\text{Fe}_3\text{O}_4$ NPs	0.0430	0.9938	0.1736	0.8454	95.24
CV- $\text{Fe}_3\text{O}_4$ NPs	0.0969	0.9730	2.2191	0.5788	99.37
MG- $\text{Fe}_3\text{O}_4$ NPs	0.0646	0.9466	0.2263	0.9867	96.23
MB- $\text{Au}@Fe_3\text{O}_4$ BNPs	0.0652	0.9892	0.3536	0.7059	97.09
CV- $\text{Au}@Fe_3\text{O}_4$ BNPs	0.1686	0.9886	3.3387	0.8832	99.11
MG- $\text{Au}@Fe_3\text{O}_4$ BNPs	0.0881	0.9717	0.5187	0.9192	98.04

proved to be the most favorable for degrading MB, CV, and MG using  $\text{Au}@Fe_3\text{O}_4$  BNPs, with corresponding  $R^2$  values of 0.9751, 0.9768, and 0.9448, respectively.

### DPPH radical scavenging activity

The DPPH radical scavenging activity of propolis extract,  $\text{Fe}_3\text{O}_4$  NPs, and  $\text{Au}@Fe_3\text{O}_4$  BNPs was evaluated. In an ethanolic solution of DPPH, there exists a  $\text{DPPH}^\bullet$  free radical, which readily accepts either an electron or hydrogen to transform into a stable diamagnetic molecule known as DPPH-H

(Hertadi et al. 2020). The introduction of propolis extract,  $\text{Fe}_3\text{O}_4$  NPs and  $\text{Au}@Fe_3\text{O}_4$  BNPs caused the donation of electrons to  $\text{DPPH}^\bullet$  free radicals, resulting in the conversion of the purple-colored free radicals into a pale yellowish DPPH-H form. Figure 14 represents UV-visible absorption plots of  $\text{DPPH}^\bullet$  scavenging using propolis extract,  $\text{Fe}_3\text{O}_4$  NPs, and  $\text{Au}@Fe_3\text{O}_4$  BNPs at various concentrations (20, 40, 60, 80, and 100  $\mu\text{g}/\text{mL}$ ), along with their respective percentages of inhibition of  $\text{DPPH}^\bullet$ . Consequently, there was a reduction in absorbance observed at 517 nm as the concentration of propolis extract,  $\text{Fe}_3\text{O}_4$  NPs and  $\text{Au}@$



**Fig. 12** (a) Variation of absorbance ( $A_t$ ) of MB, CV, and MG dye degradation with time; (b) pseudo-second-order kinetics of MB, CV, and MG dye degradation by  $Fe_3O_4$  NPs; (c) Variation of absorbance ( $1/A_t$ ) of MB, CV, and MG dye degradation with time; (d) pseudo-first-order kinetics of MB, CV, and MG dye degradation by  $Fe_3O_4$  NPs

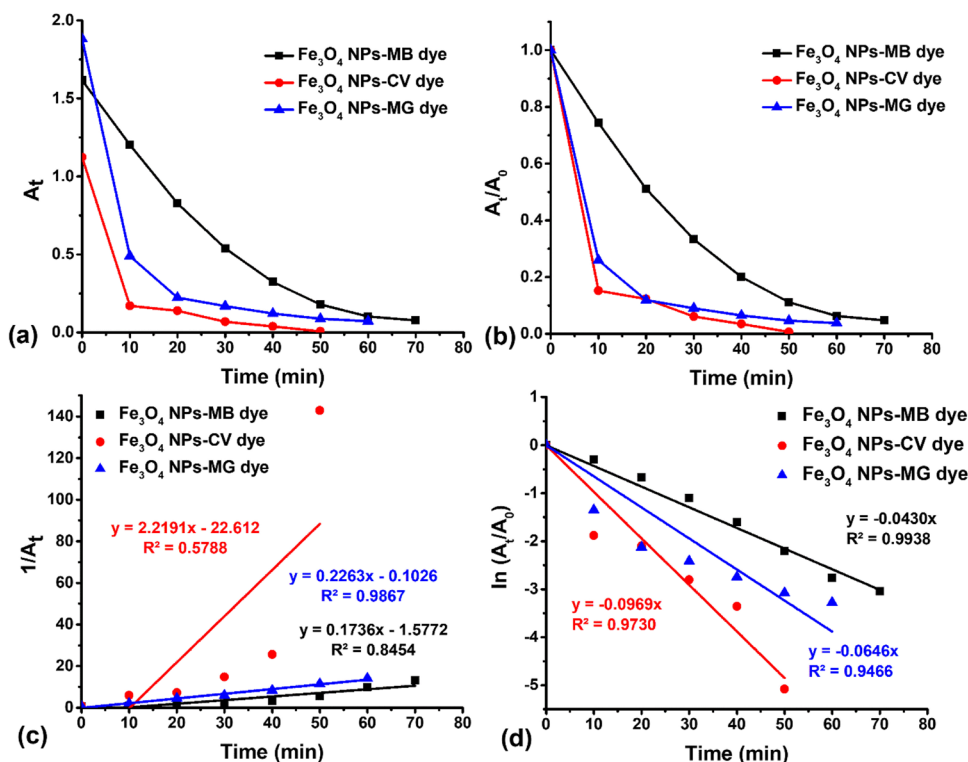
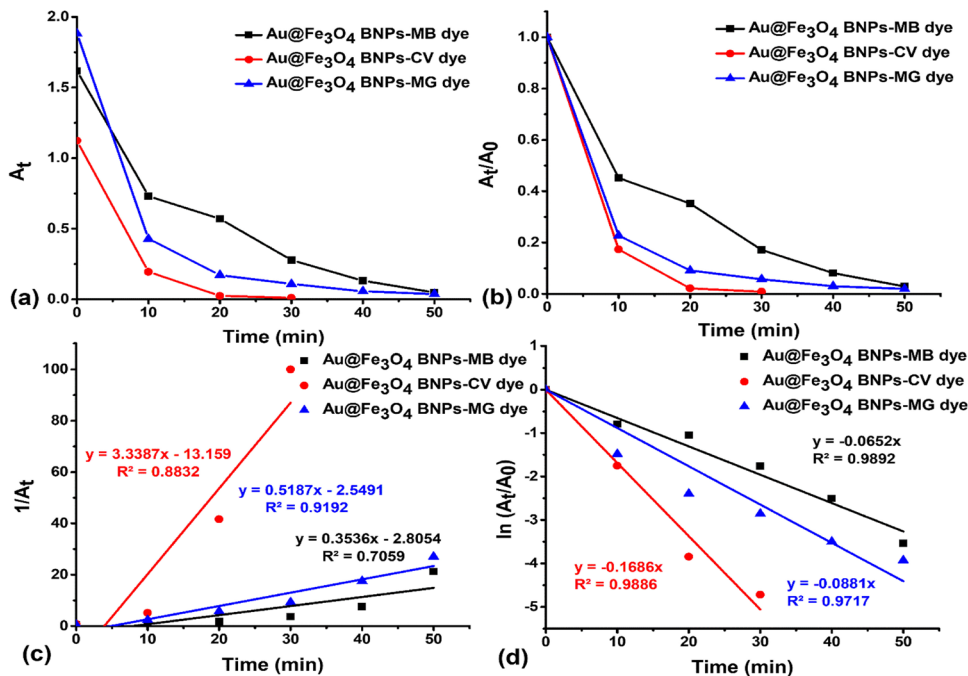


**Fig. 13** (a) Variation of absorbance ( $A_t$ ) of MB, CV, and MG dye degradation with time; (b) pseudo-second-order kinetics of MB, CV, and MG dye degradation by  $Au@Fe_3O_4$  BNPs; (c) Variation of absorbance ( $1/A_t$ ) of MB, CV, and MG dye degradation with time; (d) pseudo-first-order kinetics of MB, CV, and MG dye degradation by  $Au@Fe_3O_4$  BNPs

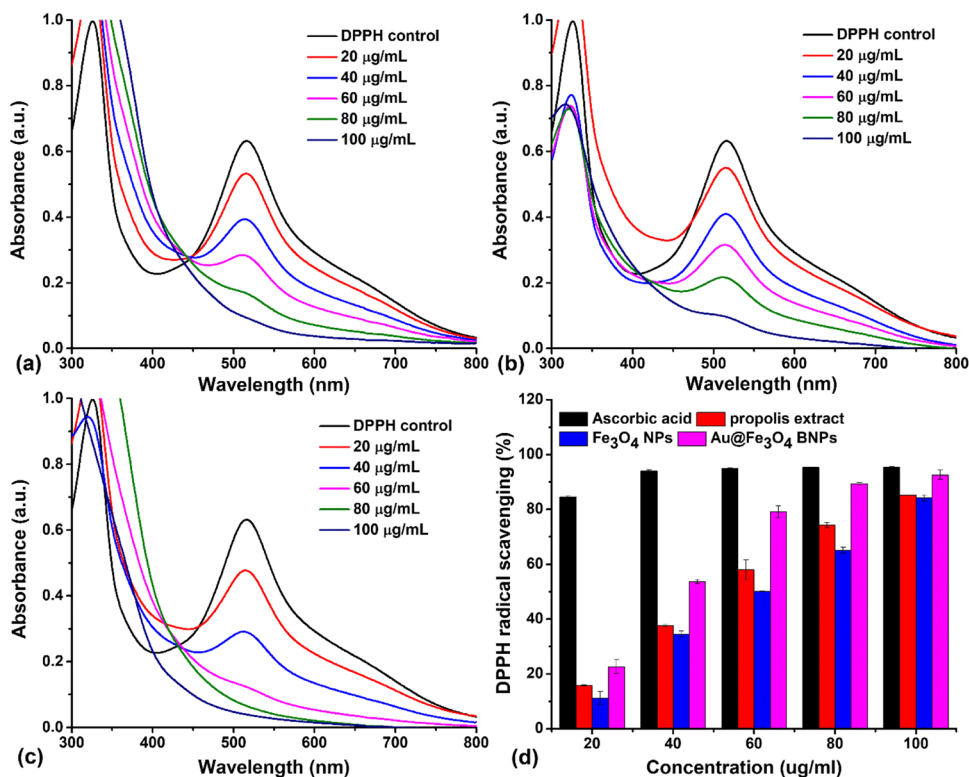


$Fe_3O_4$  BNPs increased. The antioxidant capacity of propolis extract,  $Fe_3O_4$  NPs and  $Au@Fe_3O_4$  BNPs exhibited an upward trend with increasing concentration, as depicted in Fig. 14d. Within the concentration range of 20–100  $\mu\text{g/mL}$ , the inhibition of DPPH $^\bullet$  free radicals increased from 15.8% to 85.2% for propolis extract, 11.2% to 84.2% for  $Fe_3O_4$  NPs,

and 22.7% to 92.6% for  $Au@Fe_3O_4$  BNPs, compared to the standard ascorbic acid (which exhibited inhibition rates between 84.5% and 95.4%). The  $IC_{50}$  values for the propolis extract,  $Fe_3O_4$  NPs and  $Au@Fe_3O_4$  BNPs in the DPPH radical scavenging method were determined to be  $55.23 \pm 0.98 \mu\text{g/ml}$ ,  $61.09 \pm 1.31 \mu\text{g/ml}$ , and  $40.08 \pm 1.94 \mu\text{g/ml}$ ,



**Fig. 14** UV-visible spectrum of DPPH• scavenging using (a) propolis extract, (b) Fe<sub>3</sub>O<sub>4</sub> NPs and (c) Au@Fe<sub>3</sub>O<sub>4</sub> BNPs; (d) Percentage inhibition of DPPH• using ascorbic acid (as standard), propolis extract, Fe<sub>3</sub>O<sub>4</sub> NPs and Au@Fe<sub>3</sub>O<sub>4</sub> BNPs. Statistical analysis: the values are presented as mean ± standard deviation



respectively. Among them, Au@Fe<sub>3</sub>O<sub>4</sub> BNPs exhibited the most potent antioxidant activity, as indicated by the lowest IC<sub>50</sub> value in the DPPH assay.

## Conclusion

A sustainable and cost-efficient approach has been utilized to produce environmentally friendly adsorbents as highly functional magnetic bimetallic NPs. Specifically, Fe<sub>3</sub>O<sub>4</sub> NPs and Au@Fe<sub>3</sub>O<sub>4</sub> BNPs were synthesized using propolis extract as both a reducing and capping agent. The UV-visible absorption spectra confirmed the presence of characteristic absorption peaks and the successful formation of these NPs. The FTIR analysis provided insights into the functional groups responsible for reducing and stabilizing the NPs. XRD analysis revealed the nature crystallinity of both Fe<sub>3</sub>O<sub>4</sub> NPs and Au@Fe<sub>3</sub>O<sub>4</sub> BNPs, with characteristic diffraction peaks matching their respective crystal structures. The VSM measurements demonstrated the supermagnetic nature of these NPs. Morphological analysis through FE-SEM and TEM showed that Fe<sub>3</sub>O<sub>4</sub> NPs had uniform spherical shapes with an average size of  $5.45 \pm 1.28$  nm, whereas Au@Fe<sub>3</sub>O<sub>4</sub> BNPs exhibited various shapes and aggregated structures with an average size of  $15.67 \pm 4.02$  nm. XPS analysis provided insights into the oxidation states and surface chemistry of Fe<sub>3</sub>O<sub>4</sub> NPs and Au@Fe<sub>3</sub>O<sub>4</sub> BNPs, further confirming the successful synthesis and the presence of functional groups

on their surfaces. The photocatalytic performance of Fe<sub>3</sub>O<sub>4</sub> NPs and Au@Fe<sub>3</sub>O<sub>4</sub> BNPs in degrading cationic dyes (MB, CV, MG) was highly efficient, with Fe<sub>3</sub>O<sub>4</sub> NPs exhibiting excellent dye removal percentages: 95.2% in 70 min for MB, 99.4% in 50 min for CV, and 96.2% in 60 min for MG. Au@Fe<sub>3</sub>O<sub>4</sub> BNPs, with their unique surface properties, also demonstrated dye removal percentages: 97.1% in 50 min for MB, 99.1% in 50 min for CV, and 98.1% in 60 min for MG. The kinetic analysis revealed that the pseudo-first-order kinetics model was the most suitable for describing the dye degradation process. Moreover, the DPPH radical scavenging assay demonstrated the antioxidant potential of propolis extract, Fe<sub>3</sub>O<sub>4</sub> NPs, and Au@Fe<sub>3</sub>O<sub>4</sub> BNPs; among these, Au@Fe<sub>3</sub>O<sub>4</sub> BNPs exhibited the highest antioxidant activity. These newly synthesized NPs hold promise for a wide range of applications, including wastewater treatment, catalysis, and biomedical fields, owing to their magnetic, catalytic, and antioxidant properties.

**Supplementary Information** The online version contains supplementary material available at <https://doi.org/10.1007/s11356-024-32775-3>.

**Acknowledgement** The authors sincerely thank the Ondokuz Mayıs University Research Foundation (BAP) for their financial support under Project No. PYO.FEN.1904.22.0014.

**Authors' contributions** GH-M performed the main laboratory experiments, analyzed data, and prepared the manuscript. MA contributed to the supervision and revision of the manuscript. GH-M and MA read and approved the final manuscript.

**Funding** Open access funding provided by the Scientific and Technological Research Council of Türkiye (TÜBİTAK).

**Data availability** Not applicable.

**Ethics declarations**

**Ethical approval** Not applicable.

**Consent to participate** Not applicable.

**Consent to publish** All authors consent to publish.

**Conflict of interest** The authors have no competing interest to declare that are relevant to the content of this article.

**Open Access** This article is licensed under a Creative Commons Attribution 4.0 International License, which permits use, sharing, adaptation, distribution and reproduction in any medium or format, as long as you give appropriate credit to the original author(s) and the source, provide a link to the Creative Commons licence, and indicate if changes were made. The images or other third party material in this article are included in the article's Creative Commons licence, unless indicated otherwise in a credit line to the material. If material is not included in the article's Creative Commons licence and your intended use is not permitted by statutory regulation or exceeds the permitted use, you will need to obtain permission directly from the copyright holder. To view a copy of this licence, visit <http://creativecommons.org/licenses/by/4.0/>.

## References

- Abdelsattar AS, Eid A, Rezk N, Hussein AH, El-Shibiny A (2022) Biosynthesis of gold nanoparticles using ethanolic propolis extract for methylene blue and Rhodamine-B removal. *Mater Lett* 327:133060
- Ahmed M, Mavukkandy MO, Giwa A, Elektorowicz M, Katsou E, Khelifi O et al (2022) Recent developments in hazardous pollutants removal from wastewater and water reuse within a circular economy. *npj Clean Water* 5(1):12
- Ali S, Sharma AS, Ahmad W, Zareef M, Hassan MM, Viswadevarayalu A et al (2021) Noble Metals Based Bimetallic and Trimetallic Nanoparticles: Controlled Synthesis, Antimicrobial and Anticancer Applications. *Crit Rev Anal Chem* 51(5):454–481
- Ali F, Akbar S, Sillanpaa M, Younas U, Ashraf A, Pervaiz M et al (2023) Recyclable Cu–Ag bimetallic nanocatalyst for radical scavenging, dyes removal and antimicrobial applications. *Chemosphere* 313:137321
- Allam BK, Musa N, Debnath A, Usman UL, Banerjee S (2021) Recent developments and application of bimetallic based materials in water purification. *Environmental Challenges* 5:100405
- Cheng X, Duan C, Yang P, Pi Y, Qi H, Sun Z, Chen S (2023) Effective adsorption of crystal violet onto magnetic nanoparticles decorated bacteria: Kinetic and site energy distribution analysis. *Process Saf Environ Prot* 173:837–846
- Das G, Seo S, Yang I-J, Nguyen LTH, Shin H-S, Patra JK (2023) Sericin mediated gold/silver bimetallic nanoparticles and exploration of its multi-therapeutic efficiency and photocatalytic degradation potential. *Environ Res* 229:115935
- Desai MP, Paiva-Santos AC, Nimbalkar MS, Sonawane KD, Patil PS, Pawar KD (2023) Iron tolerant Bacillus badius mediated bimetallic magnetic iron oxide and gold nanoparticles as Doxorubicin carrier and for hyperthermia treatment. *Journal of Drug Delivery Science and Technology* 81:104214
- Devi D, Muhd Julkapli N, Sagadevan S, Rafie Johan M (2023) Eco-friendly green synthesis approach and evaluation of environmental and biological applications of Iron oxide nanoparticles. *Inorg Chem Commun* 110700
- Díez AG, Rincón-Iglesias M, Lanceros-Méndez S, Reguera J, Lizundia E (2022) Multicomponent magnetic nanoparticle engineering: the role of structure-property relationship in advanced applications. *Materials Today Chemistry* 26:101220
- Foroutan R, Peighambaroust SJ, Peighambaroust SH, Pateiro M, Lorenzo JM (2021) Adsorption of Crystal Violet Dye Using Activated Carbon of Lemon Wood and Activated Carbon/Fe<sub>3</sub>O<sub>4</sub> Magnetic Nanocomposite from Aqueous Solutions: A Kinetic, Equilibrium and Thermodynamic Study *Molecules* 26(8):2241
- Hertadi R, Amari MMS, Ratnaningsih E (2020) Enhancement of antioxidant activity of levan through the formation of nanoparticle systems with metal ions. *Heliyon* 6(6):e04111
- Idris DS, Roy A (2023) Synthesis of Bimetallic Nanoparticles and Applications: An Updated Review. *Crystals* 13(4):637
- Kumar P, Dixit J, Singh AK, Rajput VD, Verma P, Tiwari KN et al (2022) Efficient Catalytic Degradation of Selected Toxic Dyes by Green Biosynthesized Silver Nanoparticles Using Aqueous Leaf Extract of Cestrum nocturnum L. *Nanomaterials* 12(21):3851
- Kwan PP, Banerjee S, Shariff M, Yusoff FM (2020) Persistence of malachite green and leucomalachite green in red tilapia (*Oreochromis hybrid*) exposed to different treatment regimens. *Food Control* 108:106866
- Laib I, Djahra Ali B, Boudebia O (2023) Green synthesis of silver nanoparticles using Helianthemum lippii extracts (HI-NPs): Characterization, antioxidant and antibacterial activities, and study of interaction with DNA. *J Organomet Chem* 986:122619
- López J, Rey A, Viñuelas-Zahinos E, Álvarez PM (2023) Preparation of a new green magnetic Fe<sub>3</sub>O<sub>4</sub>@TiO<sub>2</sub>-P25 photocatalyst for solar advanced oxidation processes in water. *Journal of Environmental Chemical Engineering* 11(3):109999
- Mani, S., & Bharagava, R. N. (2016). *Exposure to Crystal Violet, Its Toxic, Genotoxic and Carcinogenic Effects on Environment and Its Degradation and Detoxification for Environmental Safety*. In W. P. de Voogt (Ed.), *Reviews of Environmental Contamination and Toxicology Volume 237* (pp. 71-104). Cham: Springer International Publishing
- Matar GH, Andac M (2023) Green synthesis of iron oxide nanoparticles using brown Egyptian propolis extract for evaluation of their antibacterial activity and degradation of dyes. *Inorg Chem Commun* 153:110889
- Mohamed SO, El-Naggar K, Khalil MMH (2022) Green Synthesis of Silver Nanoparticles using Egyptian Propolis Extract and its Antimicrobial Activity. *Egypt J Chem* 65(7):453–464
- Moskvin M, Huntošová V, Herynek V, Matouš P, Michalcová A, Lobaz V et al (2021) In vitro cellular activity of maghemite/cerium oxide magnetic nanoparticles with antioxidant properties. *Colloids Surf B: Biointerfaces* 204:111824
- Naraginti S, Li Y (2017) Preliminary investigation of catalytic, antioxidant, anticancer and bactericidal activity of green synthesized silver and gold nanoparticles using Actinidia deliciosa. *J Photochem Photobiol B Biol* 170:225–234
- Nath D, Singh F, Das R (2020) X-ray diffraction analysis by Williamson-Hall, Halder-Wagner and size-strain plot methods of CdSe nanoparticles- a comparative study. *Mater Chem Phys* 239:122021
- Oladoye PO, Ajiboye TO, Omotola EO, Oyewola OJ (2022) Methylene blue dye: Toxicity and potential elimination technology from wastewater. *Results in Engineering* 16:100678
- Purkait PK, Majumder S, Roy S, Maitra S, Chandra Das G, Chaudhuri MG (2023) Enhanced heterogeneous photocatalytic degradation of florasulam in aqueous media using green synthesized TiO<sub>2</sub>

- nanoparticle under UV light irradiation. *Inorg Chem Commun* 155:111017
- Radoń A, Włodarczyk A, Sieroń Ł, Rost-Roszkowska M, Chajec Ł, Łukowiec D et al (2023) Influence of the modifiers in polyol method on magnetically induced hyperthermia and biocompatibility of ultrafine magnetite nanoparticles. *Sci Rep* 13(1):7860
- Rahman A, Chowdhury MA, Hossain N (2022) Green synthesis of hybrid nanoparticles for biomedical applications: A review. *Applied Surface Science Advances* 11:100296
- Rajan A, Sharma M, Sahu NK (2020) Assessing magnetic and inductive thermal properties of various surfactants functionalised Fe<sub>3</sub>O<sub>4</sub> nanoparticles for hyperthermia. *Sci Rep* 10(1):15045
- Ravelo-Nieto E, Ovalle-Serrano SA, Gutiérrez-Pineda EA, Blanco-Tirado C, Combariza MY (2023) Textile wastewater depuration using a green cellulose based Fe<sub>3</sub>O<sub>4</sub> bionanocomposite. *Journal of Environmental Chemical Engineering* 11(2):109516
- Shalaby SM, Madkour FF, El-Kassas HY, Mohamed AA, Elgarahy AM (2021) Green synthesis of recyclable iron oxide nanoparticles using *Spirulina platensis* microalgae for adsorptive removal of cationic and anionic dyes. *Environ Sci Pollut Res* 28(46):65549–65572
- Sharma G, Kumar A, Sharma S, Naushad M, Prakash Dwivedi R, Alothman ZA, Mola GT (2019) Novel development of nanoparticles to bimetallic nanoparticles and their composites: A review. *Journal of King Saud University - Science* 31(2):257–269
- Shinde BH, Shinde PB, Inamdar AK, Patole SP, Inamdar SN, Chaudhari SB (2023) Recent trends in biosynthesis of metal nanoparticles for the environmental applications. *Materials Today: Proceedings*
- Younas F, Mustafa A, Farooqi ZUR, Wang X, Younas S, Mohy-Ud-Din W et al (2021) Current and Emerging Adsorbent Technologies for Wastewater Treatment: Trends, Limitations, and Environmental Implications. *Water* 13(2):215
- Zhang N, Qiu Y, Sun H, Hao J, Chen J, Xi J et al (2021) Substrate-Assisted Encapsulation of Pd-Fe Bimetal Nanoparticles on Functionalized Silica Nanotubes for Catalytic Hydrogenation of Nitroarenes and Azo Dyes. *ACS Applied Nano Materials* 4(6):5854–5863
- Zhang J, Zhao Y, Wu S, Jia G, Cui X, Zhao P, Li Y (2022) Enhanced adsorption of malachite green on hydroxyl functionalized coal: Behaviors and mechanisms. *Process Saf Environ Prot* 163:48–57

**Publisher's note** Springer Nature remains neutral with regard to jurisdictional claims in published maps and institutional affiliations.